Politecnico di Torino

Master's Degree Thesis in Biomedical Engineering

Academic Year 2024/2025
Graduation Session December 2025

Temperature Reconstruction in Microwave Hyperthermia

Advisor:
Prof. Giuseppe Vecchi

Co-advisors:
Eng. Maryam Firuzalizadeh
Dr. Rossella Gaffoglio
Dr. Giorgio Giordanengo
Dr. Marco Righero

Candidate:
Andrea Pagnotta

Abstract

Microwave hyperthermia (HT) is a clinically validated adjunct to radio- and chemotherapy: by raising tumor temperature using non-ionizing electromagnetic fields, it increases radiosensitivity and improves intratumoral drug delivery without adding significant toxicity. Achieving effective yet safe heating requires accurate control of the spatial temperature distribution. Inadequate heating of tumor tissue reduces treatment efficacy, whereas excessive heating of healthy tissues may cause irreversible damage. Reliable temperature monitoring is therefore critical for both safety and effectiveness in hyperthermia treatments. In current clinical practice, especially for deeper targets, temperature monitoring mainly relies on catheter-based invasive thermometry, which samples only a few measurement points. Since catheter placement causes discomfort and procedural burden, their number must be minimized preventing a comprehensive characterization of the temperature distribution within the region of interest (ROI). Moreover, non-invasive alternatives such as magnetic resonance thermometry (MRT), are under development but remain limited by motion sensitivity and susceptibility artifacts, and are often difficult to implement in routine practice due to cost and logistical constraints. A recently proposed method has shown that combining sparse temperature measurements with a precomputed simulation library can enable real-time reconstruction of 3D temperature maps across the ROI. The library is generated pre-treatment from patient-specific multiphysics simulations that account for uncertainty in tissue properties. During therapy, limited measurements from minimally invasive catheters are matched to this library, reducing uncertainty and delivering a reliable, real-time 3D reconstruction of the temperature distribution. In this thesis, this reconstruction strategy is validated within the standardized benchmark framework released by the European Society for Hyperthermic Oncology (ESHO). Specifically, the ESHO ‘Alex’ head-and-neck model, which includes a nasopharyngeal tumor, is used together with the corresponding benchmark applicator, in strict accordance with the ESHO guidelines for numerical simulation and verification in hyperthermia treatment planning (HTP). The reconstruction method was tested for multiple catheter configurations and positions. Relying on a limited set of noisy invasive measurements, the reconstructed temperature map exhibited a low average error, remaining below 0.2 °C in 95% of the ROI. Encouraging performance was maintained even with reduced invasiveness: using a purely nasal, non-invasive configuration, the mean error stayed below 0.4 °C in 95% of the ROI. These results indicate that accurate temperature monitoring can be achieved with minimal or no invasive probing, underscoring the robustness of this reconstruction approach. This validation has demonstrated that the proposed reconstruction method complies with the established ESHO standards within the HT community.

Acknowledgements

The author would like to express sincere gratitude to his supervisor, Prof. Giuseppe Vecchi, who welcomed his request to join this project from the very beginning.

This work was carried out in collaboration with LINKS Foundation, and the author wishes to thank his co-supervisors Dr. Rossella Gaffoglio, Dr. Giorgio Giordanengo, and Dr. Marco Righero for their availability and support throughout the project. A special acknowledgment goes to Eng. Maryam Firuzalizadeh for her continuous supervision, particularly during the final phase of this work.

The author also acknowledges ZMT Zurich MedTech for providing access to the *Sim4Life* software under a research license agreement.

Finally, the author would like to thank Kemal Sumser for providing the ESHO model of Alex and the associated dataset, both of which were fundamental for the aims of this thesis.

Contents

Introduction 1

1 Hyperthermia Status Quo 3

1.1 Clinical Techniques . . . 3

1.2 Hyperthermia biological effects . . . 7

1.3 Mathematical model . . . 7

1.3.1 Electromagnetic Equations . . . 8

1.3.2 Thermal Modeling . . . 9

1.4 Hyperthermia treatment planning . . . 10

1.5 Critical Points . . . 12

1.5.1 Tissues properties uncertainty . . . 12

1.5.2 Invasiveness of catheter measurements . . . 13

2 Numerical Setup 15

2.1 Patient Model . . . 15

2.2 Simulation Modeling . . . 18

2.2.1 Material Properties . . . 18

2.2.2 EM Modeling . . . 19

2.2.3 Thermal Modeling . . . 21

2.3 Optimization Benchmark . . . 22

2.4 SAR and Temperature Distributions . . . 23

3 Temperature Reconstruction 27
3.1 SAR-Based Optimization 27
3.2 Reconstruction Method Workflow 31
3.2.1 Relevant Tissues 32
3.2.2 Parameters Space and Multigrid Creation 34
3.2.3 Temperature Maps Extraction 35
3.3 Reconstruction Process 36

4 Results 39
4.1 Catheter Cases 39
4.2 Reconstruction Error 41

Discussion 47

Conclusions 49

Bibliography 51

Introduction

One of the most challenging issues of medical science over the centuries has been, and still is, cancer and its treatment. In contemporary clinical practice, tumors are managed through surgery, chemotherapy, radiotherapy, or combinations thereof. Although cytostatic drugs and ionizing radiation are highly effective, they also exhibit significant side effects and an overall decrease in patients' quality of life. Fatigue, tissue injury, and systemic toxicity are among the most common complications, and combined modality therapy (chemoradiation) can become exceedingly hazardous when dose intensity is heightened in an effort to accomplish maximal tumor reduction. In order to minimize side effects and achieve a more favorable control of toxicity, among modern oncologic treatments one of the most promising is hyperthermia (HT), one of the oldest cancer treatments known, which consists in selective heating of tumor tissues to 40 - 44 °C [1]. HT is a powerful radio- and chemosensitizer that can provide substantial clinical benefit across a wide range of tumors, while enabling reductions in the dose of ionizing radiation and/or cytotoxic chemotherapy. However, a major limitation of hyperthermia—and of thermal therapies in general—is the absence of a clinically established method to non-invasively obtain a real-time temperature map of the entire heated volume. In current clinical practice, temperature monitoring is therefore typically limited to invasive thermometry, performed with only a few catheters [2]. Non-invasive alternatives, such as magnetic resonance thermometry (MRT), are under active development [3], but they are still hindered by motion sensitivity, susceptibility artifacts, high cost, and practical constraints, which limit their applicability in many treatment settings. A recently proposed approach addresses this lack of real-time volumetric thermometry by combining sparse temperature measurements with a library of pre-computed temperature simulations [4]. In this framework, a patient-specific library of multiphysics simulations is generated prior to treatment, incorporating uncertainties in tissue properties. During treatment, the limited temperature data obtained from minimally invasive or intraluminal catheters are used to identify the best-matching simulation, thereby reducing uncertainty and enabling a reliable reconstruction of the 3D temperature distribution within the ROI in real time. The European Society for Hyperthermic Oncology (ESHO) has introduced benchmark models [1] that define anatomical geometries, dielectric and thermal parameters, and standardized evaluation criteria to ensure the reproducibility and comparability of numerical studies. In this thesis, we validate the reconstruction method proposed in [4] using the ESHO “Alex” head-and-neck benchmark model, strictly following the ESHO guidelines. First, the benchmark model was fully reproduced, and the SAR-based optimization strategy described in [5] was applied to tune antenna amplitudes and phases, maximizing SAR in the tumor while limiting heating in surrounding healthy tissues. In practice, this approach provides improved SAR focusing in the tumor compared to the temperature-optimization strategy originally described in the ESHO benchmark specification. After successfully reproducing the benchmark performance in accordance with ESHO standards, the reconstruction method was implemented and evaluated. Several catheter placement configurations, including minimally invasive ones, were examined to assess the robustness of the approach. The results indicate that the reconstruction method can reliably approximate the full 3D temperature distribution, supporting its potential for safe and effective integration into standard clinical hyperthermia workflows.

Chapter 1

Hyperthermia Status Quo

Hyperthermia (HT) is an adjuvant treatment used in cancer therapy involving the controlled increase of temperature in selected biological tissues and is yielding promising results across a wide range of oncologic applications. It is a very ancient approach: it is reported as early as around 5000 BC in the Edwin Smith Surgical Papyrus. The ancient Indian medical treatises Charaka Samhita and Sushruta Samhita, which were composed around 3000 BC, also had mentioned hyperthermia as a therapeutic method [6] while back in ancient Greece, Hippocrates supposedly used to treat superficial tumors by cauterizing them with hot iron [7]. In 1866 the German surgeon Carl D. W. Busch reported the case of a 43-year-old female patient with facial sarcoma whose tumor regressed after a fever occurring postoperatively [8]. This was the first verifiable evidence that increased temperature could selectively damage malignant tissue without the same amount of damage to normal tissue. This observation has drawn attention to hyperthermia, and thanks to significant technological developments in non-ionizing radiation during the final decades of the twentieth century, the clinical adoption of thermal therapies has been facilitated. HT is actually achieved by exposing tissue to acoustic or non-ionizing electromagnetic (EM) radiation – e.g. microwaves or radiofrequency - thereby raising the temperature of the tumor site. The increase in temperature can lead to selective damage or death of tumor cells, which are more vulnerable to thermal stress than healthy cells [7].

1.1 Clinical Techniques

HT is currently used, typically in combination with chemotherapy and radiotherapy, for several advanced cancers, including recurrent lung, prostate, rectal, head-and-neck (H&N), uterine and breast cancer. Indeed, HT can enhance the effectiveness of ionizing radiation and cytotoxic drugs, and its coupling with these therapies can significantly improve treatment outcomes [7]. The therapeutic objective is to elevate intratumoral temperature to make tumor-cells more sensitive to radiotherapy and chemotherapy. In standard practice, HT is administered for approximately 60 minutes before or following radiotherapy within a 0.5–4-hour time window; concurrently with chemotherapy, or shortly after completion of the drug course [9]. Clinical outcomes are highly sensitive to heating time, thermal dose, and ability to accurately control temperature in the ROI [10]. During clinical practice, the ability to deliver the desired heating time and thermal dose depends strongly on the target anatomy, especially its size, location and depth. Heating can be delivered either internally or externally. Internal hyperthermia is achieved via interstitial, intraluminal, or intracavitary approaches using ultrasound, radiofrequency (RF) or microwave (MW) applicators [6]. By contrast, external hyperthermia depends strongly on the target volume and anatomical site, with the choice of applicators and heating method tailored to the region of interest. External techniques are commonly grouped into two broad categories, as shown in Figure 1.1:

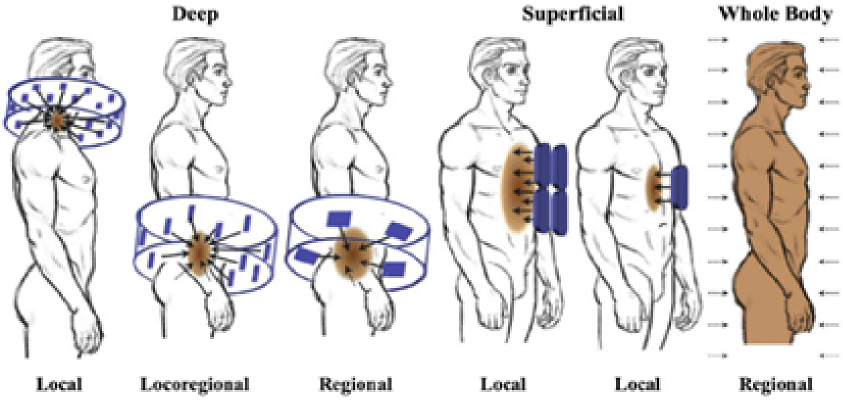

Figure 1.1: Overview of external electromagnetic-based hyperthermia techniques for cancer treatment [9].

1. Superficial Hyperthermia: consists in heating of tissues or tumors typically located within a few centimeters from the skin. Generally, target regions are treated with higher MW frequencies, either at 434 MHz or 915 MHz [9].

2. Deep Hyperthermia: designed for tumors located at deeper regions of the body (more than 4cm from the skin's surface). In this case, operating frequencies lie in the 1–1000 MHz range and the temperature goal is often better achieved with a phased-array approach, where an array of antennas is placed around the patient [9].

Depending on the clinical scenario, external heating may be delivered using different approaches:

- Local Hyperthermia: the target is a very specific portion of the body, so a tumor or group of tumors localized in the same area. Most used forms of energy in this treatment are ultrasound (US) waves or electromagnetic radiation such as microwaves and radio waves [9].
- Regional Hyperthermia: deals with targeting a specific area of the body, larger than the previous case. The goal is to target a group of organs or tissues over a relatively wide region, without affecting the rest of the patient's body [9].
- Whole-body hyperthermia: consists in raising the temperature of the entire patient's body. Techniques involved are infrared radiation, heated air, or warm water immersion, aiming at arising temperature above physiological level [11].

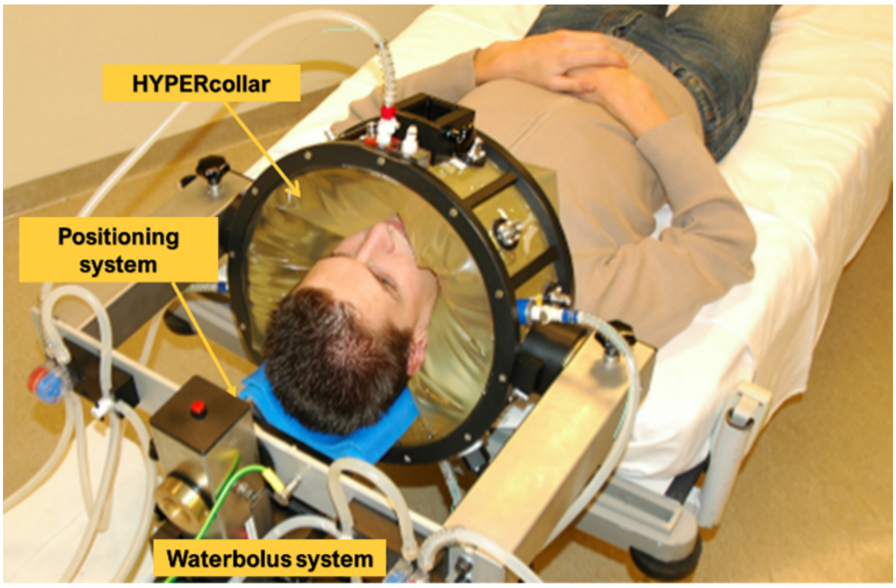

Figure 1.2: HYPERcollar setup for Head and Neck tumor [12].

Over the years, several tools and devices have been developed aimed at improving the above-mentioned techniques. This thesis concerns H&N cancer, where the applied heating modality is deep localized hyperthermia. An example of H&N applicator is the HYPERcollar, developed by Paulides et al [13] and mentioned in ESHO benchmark as a reference applicator. The HYPERcollar is a transparent Perspex (PMMA) cylinder covered with a fine conducting gauze forming the conducting backplanes required for a variable number of patch antennas, arranged on two circular rings and operating at 434 MHz (Figure 1.2). The HYPERcollar comprises an inflatable waterbolus, which consists of a circular reservoir of demineralized water placed in between the neck of the patient and the antennas. This water layer serves multiple purposes: it enables an efficient transfer of electromagnetic waves coming from the antennas into the patient while at the same time cooling the skin to prevent superficial hot spots. The whole applicator is also equipped with a positioning system, since it is fixed on a trolley that can be moved and rotated around the axis of the patient, offering maximal flexibility in positioning. However, in this thesis the applicator used is the benchmark applicator proposed by ESHO for the H&N region [1], which was developed from simplified versions of the two reference applicators: the HYPERcollar, described above, and the HYPERcollar3D [12]. The benchmark applicator therefore combines features of both reference designs - number of antennas, overall geometry and shape, inter-antenna spacing - which will be discussed in Section 2.1. Several studies and experimental tests have established that the 400–600 MHz range is suitable for efficiently focusing energy toward the center of the neck. The choice of 434 MHz represents the best compromise, since at this frequency power focusing improves as the number of antennas and rings increases [12].

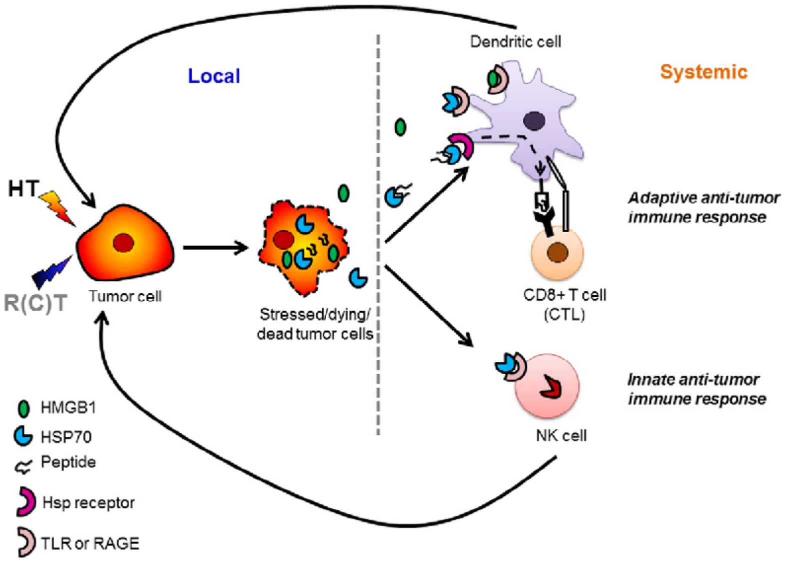

Figure 1.3: When heated, tumor cells release danger signals (e.g. HMGB1), heat-shock proteins such as HSP70, and tumor-derived peptides. These mediators are recognized and internalized by dendritic cells (DCs) through specific receptors (e.g. HSP receptors, TL TLR/RAGE), promoting DCs maturation. Then, DCs process the peptides and cross-present the corresponding tumor antigens on MHC class I to CD8^{+} cytotoxic T lymphocytes (CTLs) with appropriate co-stimulation. HMGB1 engages DCs through receptors, enhancing antigen cross-presentation, while danger signals may also activate natural killer (NK) cells. Their activity, combined with CTLs' one, culminates in tumor cell lysis [6].

1.2 Hyperthermia biological effects

Besides the technical aspects of energy delivery, hyperthermia exerts a range of biological effects on tumors and their microenvironment that are crucial for its clinical efficacy. Recent evidence shows that deep localized hyperthermia is able to induce systemic anti-tumor immune responses, providing several effects on the tumor environment [6], such as:

- Sensitization of cells in S phase (DNA-synthesis phase of the cell cycle, during which replicating cells are particularly vulnerable to certain therapies).
- Local phenotypic remodeling of tumor cells and their micro-environment which might increase the tumor immunogenicity.
- Imposing thermal stress on tumor cells, driving them toward immunogenic cell death. This process is called "in situ tumor vaccination" (Figure 1.3)

In addition to stimulating the body's natural immune response, it has been proven that hyperthermia substantially enhances the effectiveness of both radiotherapy and chemotherapy in treatment of primary and recurrent tumors [14]. From a biological perspective, hyperthermia:

- Interferes with DNA repair, thereby intensifying the damage from radiation and drugs.
- Improves tumor perfusion and oxygenation, reducing hypoxia, which is one of the major causes of radioresistance.
- Increases drug uptake in tumor tissue.

All these important attributes support adding hyperthermia to combined treatment, offering a clear biological reason to use it alongside radiotherapy and chemotherapy, with synergy that varies according to treatment timing.

1.3 Mathematical model

Successful hyperthermia treatments are tightly linked to the underlying mathematical modeling. Such modeling is the core that connects device settings to biological effect, making hyperthermia predictable, safe, and optimizable. It is therefore essential for turning a heat source into an accurate, patient-specific therapy. Since treatment efficacy depends on how electromagnetic energy is deposited and converted into heat, the mathematical model must capture both electromagnetic and thermal phenomena.

1.3.1 Electromagnetic Equations

Electromagnetic heating is one of the most effective methods used for hyperthermia. Its adoption is supported by several advantages, especially when using radiofrequency RF or MW radiation, as in this project. These radiations are non-ionizing and, combined with the non-invasive nature of the heating approach, markedly reduce risks to patient safety. Moreover, RF/MW energy enables uniform and spatially controllable heating, which is essential for achieving precise targeting of the anatomical region of interest [15]. Since EM wave propagation arises from the coupled dynamics of the electric and magnetic fields, it is important to outline their mutual interactions, which are described in Maxwell's equations [16]:

$$\nabla \cdot \mathbf{E} = \frac{\rho}{\varepsilon} \qquad \text{Gauss's law for electric field} \tag{1.1}$$

$$\nabla \times \mathbf{E} = -\frac{\partial \mathbf{B}}{\partial t} \qquad \text{Faraday's induction law} \tag{1.2}$$

$$\nabla \cdot \mathbf{B} = 0 \qquad \text{Gauss's law for magnetic field} \tag{1.3}$$

$$\nabla \times \mathbf{B} = \mu \left(\mathbf{J} + \varepsilon \frac{\partial \mathbf{E}}{\partial t} \right) \qquad \text{Ampère's circuital law} \tag{1.4}$$

In the first equation (1.1), $\mathbf{E}$ is the electric field (V/m), ρ is the charge density (C/m^3), while ε is the dielectric permittivity (F/m). In equations (1.2) and (1.3), $\mathbf{B}$ is the magnetic field (T). Finally, in equation (1.4), μ is the magnetic permeability (H/m) and $\mathbf{J}$ is the electric current density (A/m^2).

In general, at low frequencies, the EM field induces conductive currents in the body, and the dominant effect is Joule heating. Above 100 MHz, the radiative propagation regime and dielectric losses become predominant. Since microwaves range from 300 MHz to 300 GHz, tissues subjected to this type of radiation can be effectively modeled as lossy dielectrics [9] in which energy absorption is governed mainly by dielectric losses rather than by conduction alone.
For this reason, within a volume V where an electromagnetic field is propagating, the power dissipation due to time-harmonic EM fields is given by:

$$\frac{dp_{\text{diss}}}{dV} = \mathbf{E}(r,t) \cdot \mathbf{J}(r,t) \tag{1.5}$$

In this equation, p_{diss} (W) is the power dissipated in the volume, while $\mathbf{E}(\boldsymbol{r},t) = \Re\{\mathbf{E}e^{j\omega t}\}$ and $\mathbf{J}(\mathbf{r},t) = \Re\{\mathbf{J}e^{j\omega t}\}$, and $\boldsymbol{r}$ is the position vector. Using the macroscopic constitutive relation $\mathbf{J} = \sigma\mathbf{E}$ [16] and taking the time average over one period T [15], equation (1.5) becomes:

$$\left\langle \frac{dp_{\text{diss}}}{dV} \right\rangle_T = \frac{1}{2}\sigma(\boldsymbol{r}) \left|\mathbf{E}(\boldsymbol{r})\right|^2 \tag{1.6}$$

Where $|\mathbf{E}|$ is the peak value of the electric field's magnitude (V/m) and σ (S/m) is the electrical conductivity. When the right term of equation (1.6) is normalized by the tissue density ρ (kg/m^3), the Specific Absorption Rate (SAR) parameter is obtained:

$$\text{SAR}(\mathbf{r}) = \frac{\sigma(\boldsymbol{r})}{2\,\rho(\boldsymbol{r})} \left|\mathbf{E}(\boldsymbol{r})\right|^2 \tag{1.7}$$

When a tissue interacts with EM waves, SAR (W/Kg) quantifies the rate of EM energy absorption per unit of mass of the tissue [1]. In addition to characterizing the relationship between electromagnetic field intensity and its effects on the target tissues, it is also a critical patient-safety parameter, as it enables assessment of exposure safety [17].

1.3.2 Thermal Modeling

Two main classes of thermal models are commonly used:

- Discrete Vasculature (DIVA) model (discrete).
- Pennes' Bioheat Equation (PBHE, continuum).

DIVA-type models explicitly represent individual blood vessels in order to capture the non-continuum nature of perfusion and non-equilibrium effects; vascular trees can be derived from MRI data, leading to physiologically realistic geometries [18], [19]. However, DIVA workflows involve many manual steps and approximations and are computationally quite demanding Consequently, during the treatment-planning phase, heat transport in the human body is typically modeled using PBHE, as it is less expensive computationally and easier to implement. The equation, originally proposed by the bioengineer Harry H. Pennes [20] and reported below, accounts for the main factors that drive temperature changes within tissues and can be directly coupled to the SAR term:

$$\rho C \frac{\partial T}{\partial t} = k\nabla^2 T + q_s \tag{1.8}$$

In the equation, for the considered tissue ρ is the tissue mass density (kg/m^3), C is the heat capacity (J/(kg · °C)), k is the thermal conductivity (W/(m · °C)), and q_s (W/m^3) is the source term, which can be expressed as:

$$q_s = q_{hs} + q_m + q_p \tag{1.9}$$

where:

- q_{hs}: heat source term, which in the context of hyperthermia coincides with the power dissipation term given in (1.6), written in terms of SAR (1.7):

$$q_{hs} = \frac{p_{\text{diss},\Omega}(t)}{dV} = \rho\, SAR \tag{1.10}$$

- q_m: heat term produced by metabolic reactions.
- q_p: heat loss term due to blood perfusion, which can be written as:

$$q_p = -\omega_{bl} C_{bl} \rho_{bl} \Big(T - T_a \Big) \tag{1.11}$$

with ω_{bl} the blood perfusion rate (ml/(kg · °C)), $C_{bl} = 3890$ J/(kg · °C) the blood specific heat, $\rho_{bl} = 1060$ kg/m^3 the blood mass density, and $T_a = 37$°C the arterial blood temperature [15]. Blood shows a compensatory behavior in response to temperature fluctuations — it removes heat when tissues' temperature increases — which accounts for the presence of the minus sign in the expression.

By explicitly substituting all the terms introduced above, expression (1.8) becomes:

$$\rho C \, \frac{\partial T}{\partial t} = k \nabla^2 T + \rho\, SAR + q_m - \omega_{bl} C_{bl} \rho_{bl} \Big(T - T_a \Big) \tag{1.12}$$

At this point, the guidelines proposed by ESHO [1] recommend omitting the metabolic heat generation term, since its effect is small relative to the EM term, so $q_m \approx 0$. In addition, ESHO advises using a steady-state formulation of the bioheat equation, so that all transient terms can be neglected ($\rho C \partial T / \partial t = 0$).

1.4 Hyperthermia treatment planning

Having established how SAR and tissue properties determine the resulting temperature field and, consequently, the clinical outcome of hyperthermia, it is now important to address how patient-specific heating strategies are designed.

The use of HT for deep-seated tumors can introduce specific challenges, including:

- Control of applicators during hyperthermia delivery.

- Real-time verification of the 3D temperature distribution within the target region [21].
- Achieving the desired optimal thermal dose for an almost hour-long HT treatment [15].

In such cases, hyperthermia treatment planning (HTP) represents a crucial approach in overcoming these clinical challenges and becomes pivotal in ensuring the safety of the patient. HTP can be defined as the process that begins with patient data acquisition and establishing, using hyperthermia applicator (e.g. EM, US) and/or thermal modeling, a set of treatment parameters that optimizes the quality of the treatment [18].

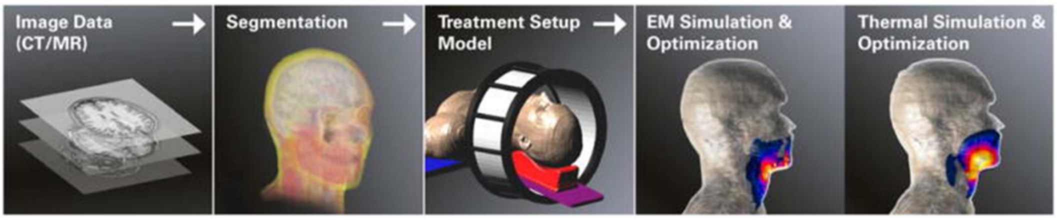

Figure 1.4: Hyperthermia treatment plan for H&N cancer workflow [18].

The success of hyperthermia is strongly dependent on the implementation of an effective HTP, whose main steps are outlined below [6], [18], with a particular focus on H&N cancer (Figure 1.4):

1. Image acquisition: First step consists of acquiring a magnetic resonance (MR) or computed tomography (CT) image with the patient in treatment position. The posture that the patient assumes during image acquisition must match the one used during HT treatment in order to avoid planning errors.
2. Tissues segmentation: Using image data, a manual, semi-automatic or automatic segmentation of different tissue types creates a full 3D patient model together with the clinical target volume (CTV) or the gross tumor volume (GTV).
3. Virtual incorporation into software: Segmented patient model, target volume and 3D model applicator are virtually inserted into the HTP software, which is based on Finite Elements (FE) or Finite-Difference Time Domain (FDTD) methods. In this phase, tissue specific EM and thermal properties are assigned.
4. SAR and temperature optimization: Applicators' amplitudes, phases, and frequencies are optimized, aiming at reaching higher temperatures in the target volume and avoiding the formation of hot spots in the surrounding healthy

regions. The various types of optimizations developed so far are divided into SAR-based and temperature-based. The former aims to maximize the ratio between the energy deposition in the target volume and that in the surrounding tissues, while the latter is designed to maximize the temperature in the target volume, imposing soft and hard constraints on both the tumor and the surrounding tissues [1].

5. Patient and thermometry setup: The patient is positioned relative to the microwave applicator according to the selected optimized setup. In addition, with the aid of a CT scan, closed-tip thermometry catheters are placed on the skin, interstitially and/or intraluminally.
6. Fiber optic sensors' insertion: Optical thermometric fibers are inserted into the interstitial and intraluminal catheters, ensuring temperature monitoring along the direction of insertion of the catheters.
7. Waterbolus filling procedure: Waterbolus is filled with circulating demineralized water, kept at constant temperature between 20 °C - 30 °C.
8. Treatment session: Optimized phases and amplitudes are transferred and applied to the patient via the HT system unit.
9. Temperature monitoring and (if necessary) treatment adjustments: If SAR or temperature thresholds are exceeded or the patient reports pain, radiation procedure is stopped. Amplitudes and phases may need to be re-optimized, particularly if a hotspot is detected.

1.5 Critical Points

Although the previous section (1.4) has described how hyperthermia can be planned and optimized in a patient-specific way, some critical points remain. In this section two of the most relevant issues are discussed: uncertainty in tissue properties used for modeling and invasiveness of catheter-based temperature monitoring in the tumor region.

1.5.1 Tissues properties uncertainty

In the previous sections (1.3.1 and 1.3.2), dielectric (electrical conductivity σ and permittivity ε) and thermal (heat capacity c, thermal conductivity k, and blood perfusion rate ω) parameters were introduced. These quantities strongly influence both the electromagnetic and thermal modeling and, consequently, the final outcome of hyperthermia treatments, especially when - as in this thesis - tissue properties assigned to the phantom are taken from literature (see Section 2.2.1). These parameters are not patient-specific, they are estimated as averages over different studies and their values can significantly change under HT treatments [4]. Hence, hyperthermia is particularly sensitive to uncertainties in tissue properties, especially thermal parameters, whose variability is considerable.

First, there is considerable inter-patient variability, as well as variability arising from experimental conditions and measurement techniques. In addition, due to the intrinsic heterogeneity of human tissues, regions with a high-water content - such as muscle - tend to absorb more electromagnetic energy and therefore heat up more than other areas [22]. Finally, all of these parameters change as a non-linear function of tissue temperature, further complicating their accurate characterization [18].

This variability in dielectric and thermal properties can lead to inaccuracies on the order of 20% in both SAR and temperature predictions [23], which represents a significant issue for hyperthermia, particularly in delicate regions such as the H&N, where thermosensitive tissues – cerebrum, spinal cord, and brainstem - are present in close proximity to the target.

For the reasons outlined above, uncertainty in tissue properties remains one of the main reasons why patient-specific thermal simulations during treatment are not sufficiently reliable per se for temperature monitoring. A central challenge in modern hyperthermia is to properly account for these uncertainties and to minimize their impact on treatment outcomes.

1.5.2 Invasiveness of catheter measurements

Conventional real-time temperature monitoring in clinical hyperthermia is based mainly on invasive thermometry, where small catheters are inserted into or near the tumor region and used as guides for thermometric probes. The probes often consist of fiber optic sensors that do not interfere with the electromagnetic field. Although this approach is still considered the reference standard for intratumoral temperature control, it is uncomfortable, often painful and associated with procedural risks for the patient [24]. Moreover, catheter-based measurements provide only sparse sampling along a few trajectories and therefore offer limited spatial information on the 3D temperature distribution [25]. A non-invasive underdevelopment alternative is magnetic resonance thermometry (MRT) [26], which can provide a full 3D temperature distribution and is associated with much lower risk for the patient. However, this technique is not yet widely applied, mainly due to the high operating costs of MR systems, besides the technical challenges for adapting hyperthermia applicators to the MR environment, considering that they are mostly designed based on metallic structures. Moreover, at current state it only provides relative temperature change data, is subject to inaccuracies due to motion (e.g. respiratory motion) and presents some difficulties in measuring fatty tissues [4]. These limitations have motivated the search for minimally invasive or non-invasive thermometry techniques that can reduce patient burden while allowing more comprehensive thermal surveillance during hyperthermia treatments.

Chapter 2

Numerical Setup

In this chapter, we describe the numerical framework adopted to model head and neck hyperthermia treatments and to reproduce the benchmark model proposed by ESHO. The workflow is based on a realistic patient model, literature-based EM and thermal tissue properties, and a coupled EM–thermal simulation pipeline.

2.1 Patient Model

The anatomical models commonly used in HTP simulation studies are computer-aided design (CAD) models of healthy volunteers and homogeneous phantoms. These CAD models are stored in a novel, openly accessible database called the Erasmus Virtual Patient Repository (EVPR) [21]. For H&N patient – such as Alex, the realistic model used in this study – model generation starts with delineating CT scans into normal tissues using a semi-automatic segmentation routine followed by a manual adjustment in dedicated software [27]. Patient models are generated in the exact same position and with the same body shape as during the hyperthermia treatment. For each realistic patient, a trained clinician identified the hyperthermia target volume (HTV) starting from the clinical target volume (CTV) or gross tumor volume (GTV) and adding certain margins that depend on the specific case [21]. The virtual patient analyzed in this thesis is Alex, based on a patient with a very challenging case of a deeper-seated nasopharynx tumor, shown in Figure 2.1, with an overall HTV of approximately 44 ml. Specifically, in this model the HTV consists of the GTV plus a surrounding margin of 10 mm.

A more comprehensive visualization of Alex is shown in Figure 2.2, where both the superficial layers and the deeper tissues, as well as the GTV, are highlighted. As can be seen in the figure, a non-isotropic volumetric expansion of the muscle tissue was introduced in the model to cover the eye region. This anonymization

Figure 2.1: Sagittal and transversal view of EVPR Alex model with only bones and GTV [21].

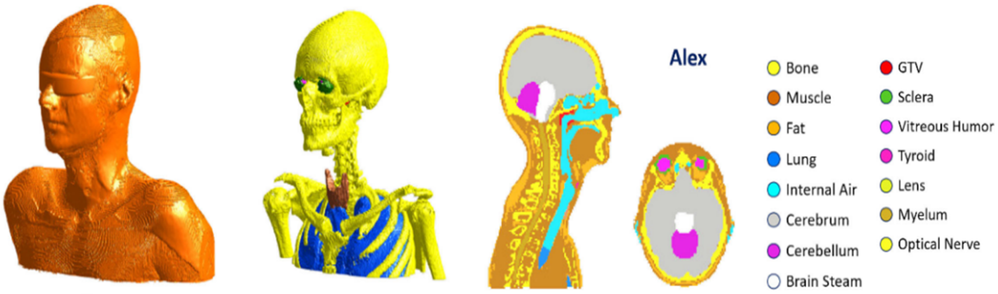

Figure 2.2: EVPR Alex model, all healthy tissues highlighted [21].

step was implemented in order to comply with current privacy regulations and to allow sharing of the considered patient models. The authors verified that the presence of this additional layer does not affect any HTP metrics [21].

Benchmark Applicator:

As already introduced in Section 1.1, the benchmark applicator proposed by ESHO [1] for the Alex model used in this work is derived from simplified versions of clinical reference applicators, whose main characteristics are summarized in Table 2.1.

The benchmark applicator consists of an array of twelve half-wavelength dipole antennas (total length 51 mm with an 8 mm feed gap) operating at 434 MHz and aligned along the z-axis (caudo–cranial direction). The antennas are distributed over three rings, spaced 4.5 cm apart, in a horse-shoe configuration so as to avoid placing antennas directly in front of the nose, chin, ears, and neck (Figure 2.3).

In this simplified configuration, the waterbolus is modelled as a cylinder with a diameter of 34 cm and a height of 16 cm, extending to cover the nose and eyes [1]. In clinical applicators, however, the bolus usually has a patient-specific, tailored shape that allows for unobstructed breathing and verbal feedback, while also helping to reduce claustrophobic sensations.

Table 2.1: Overview of reference and benchmark applicators [1].

Reference applicator 1	Reference applicator 2	Benchmark applicator
HyperCollar	HyperCollar3D	H&N applicator
434 MHz	434 MHz	434 MHz
Cylindrical shape	Horse-shoe shape	Horse-shoe shape
12 patch antennas	20 patch antennas	12 dipole antennas
2 antenna rings	3 antenna rings	3 antenna rings
Equidistantly spaced	Non-equidistant	Non-equidistant

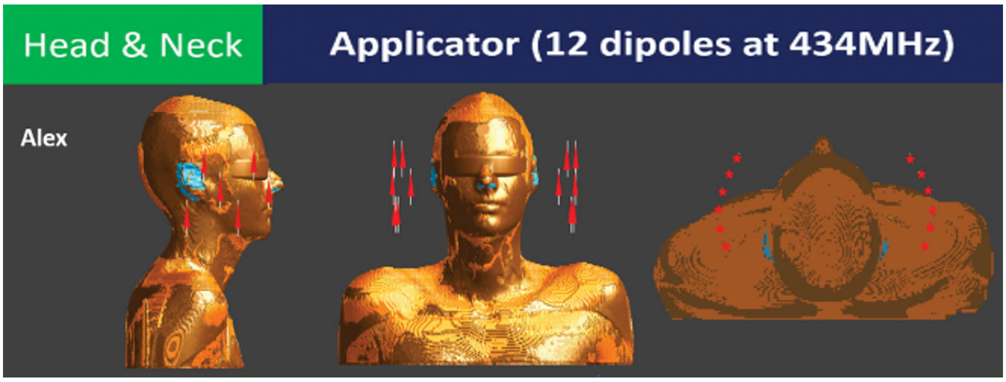

Figure 2.3: Benchmark H&N applicator for Alex model [1].

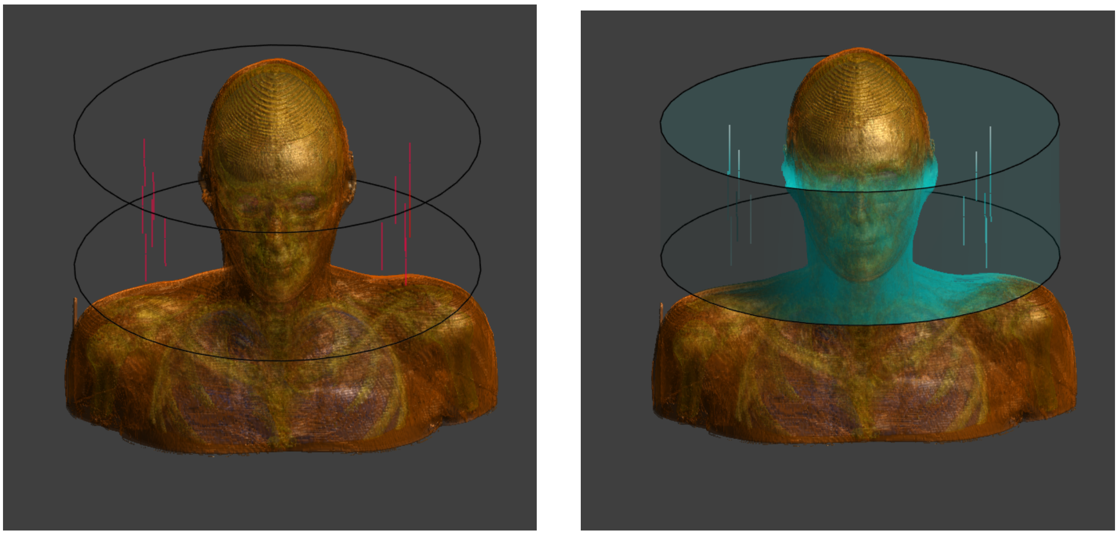

(a) (b)

Figure 2.4: Alex model imported in Sim4Life: visualization with antennas (a) and with waterbolus (b).

2.2 Simulation Modeling

In this section, we describe the numerical framework adopted for the EM and thermal simulations and for the analysis of the corresponding results. The Alex model was first imported into the simulation software Sim4Life [28] (Figure 2.4 a , b), which provides a full-wave electromagnetic solver coupled to a biothermal solver capable of solving the PBHE (1.12). All simulations were performed in the Sim4Life environment, where the dielectric and thermal tissue properties were assigned, while post-processing and quantitative analysis of the resulting SAR and temperature distributions were carried out in MATLAB [29].

2.2.1 Material Properties

To obtain a realistic representation of the treatment scenario, it is essential to account for temperature changes driven by physiological thermoregulation, which itself depends on the electrical and thermal properties of tissues. While electrical properties directly control the absorption of electromagnetic energy and therefore the local rate of heat deposition, thermal properties and blood perfusion determine how this heat is redistributed within the tissue. Consequently, these parameters play a pivotal role in both pre-clinical and clinical applications based on electromagnetic energy for heating [30].

Table 2.2: Dielectric properties of healthy tissues [31] and tumor [32] at the operating frequency of 434 MHz.

Tissue	Relative permittivity (-)	Electrical conductivity (S/m)
Bone	13,07	0,094
Fat	11,59	0,082
Muscle	56,87	0,805
Lung	23,58	0,380
Cerebellum	55,11	1,048
Cerebrum	56,81	0,751
Brain stem	55,11	1,048
Spinal cord	35,04	0,456
Eye (sclera)	57,37	1,004
Eye (lens)	37,29	0,379
Vitreous humor	69,00	1,534
Cartilage	45,14	0,598
Thyroid	61,33	0,886
Optical nerve	35,04	0,456
Tumor	57,20	0,884
Blood	63,83	1,361

Table 2.3: Thermal properties of healthy and tumor tissues at baseline [31] and under thermal stress [33]. Blood perfusion rates are presented in ml/(min kg) for convenience.

Tissue	Density (kg/m^3)	Specific heat capacity (J/(kg °C))	Thermal conductivity (W/(m °C))	Blood perfusion rate (ml/(min kg))
Bone	1908	1313	0.32	10.0
Fat	911	2348	0.21	32.7 / 69.0*
Muscle	1090	3421	0.49	36.7 / 188.7*
Lung	394	3886	0.39	400.9
Cerebellum	1045	3653	0.51	770.0
Cerebrum	1045	3696	0.55	763.3
Brain stem	1046	3630	0.51	488.0
Spinal cord	1075	3630	0.51	160.3
(Eye) Sclera	1032	4200	0.58	380.0
(Eye) Lens	1076	3133	0.43	N/A
Vitreous humor	1005	4047	0.59	N/A
Cartilage	1100	3568	0.49	35.0
Thyroid	1050	3609	0.52	5624.3
Optical nerve	1075	3613	0.49	160.3
Tumor	1090	3421	0.49	N/A / 94.4*
Internal air	1	10040**	0.03	N/A
Blood	1050	3617	0.32	N/A

(*) Tissue properties under stress. (**) The specific heat capacity of air is increased by a factor of 10, as later will be discussed in Section 2.2.3.

The dielectric and thermal tissue properties used in this work were adopted from the ESHO guidelines [1] to adhere strictly to the benchmark protocol. These properties were mostly extracted from the IT'IS Tissue Properties Database [31], a continuously updated online resource for human EM and thermal modeling. However, this database includes only healthy tissue properties at baseline temperature and does not provide values for malignant tissues or under thermal stress. Due to this limitation, malignant tissue dielectric properties were taken from [32], whereas thermal properties under thermal stress were obtained from [33]. The dielectric and thermal properties used in this thesis' simulations are reported, respectively, in Table 2.2 and Table 2.3.

2.2.2 EM Modeling

To perform the EM simulations, the Electromagnetic Finite-Difference Time-Domain (EM-FDTD) solver available in Sim4Life was employed. A multiport excitation scheme was used, in which Maxwell's equations are solved multiple times while driving only one antenna at a time. After assigning the dielectric properties to each tissue as described in Section 2.2.1, the EM simulations were carried out in accordance with the ESHO benchmark guidelines [1]:

- Antennas are excited with harmonic signals and simulated for at least 20 periods.
- The frequency of harmonic excitation signals is 434 MHz, with a reference load of 50 Ohm.
- For metallic regions, perfect electric conductor (PEC) material must be assigned.
- Computational domain has to be terminated using a global absorbing boundary condition (ABC) with uniaxial perfectly matched layers (UPML) to suppress artificial reflections of the electromagnetic field at the outer boundaries.
- For H&N models, it is recommended to use a maximum grid step of 1.5 mm for tissues and 0.75 mm for the benchmark HT applicator.

Besides the spatial steps described above, a maximum grid step of 2.5 mm was imposed in the waterbolus and in a dedicated volume-of-interest (VOI) sensor, defined as a box enclosing only the head and neck portion of the Alex model. Such VOI allowed an easier extraction of the results of the simulation, excluding regions of minor interest and providing lighter and more easily manageable output files in post-processing.
To further reduce the overall computational burden, the maximum grid step in the tissue region was relaxed to 2.5 mm, while a finer limit of 1.25 mm was retained in the applicator region, yielding a final grid of approximately 19.85 Million cells.
A voxelization step was performed once the grid was defined, prior to running the EM-FDTD solver. In Sim4Life, each solid of the model is represented by a surface triangle mesh, which is combined with the grid in order to generate the voxel representation of all entities within the computational domain.

Once the EM simulations were completed, the derived fields for the individual antenna excitations were combined in Sim4Life using the Simulation Combiner tool, which linearly superimposes the contribution of each antenna. In this step, the feeding coefficients (amplitude and phase) for the twelve antennas are assigned according to the benchmark optimization [1], which will be discussed in Section 2.3.

2.2.3 Thermal Modeling

After EM simulation was performed, the thermal solver was employed to solve the PBHE (1.12). For the thermal simulations, the source term corresponds to the electromagnetic energy absorbed by the tissues, quantified by the SAR and converted into volumetric heat generation. In Sim4Life, this quantity is represented by the power loss density (PLD, W/m^3), which is extracted from the EM solution, stored as a cache file in a dedicated folder, and subsequently used as the input source term for the thermal simulations.
During heating, local perfusion values can be significantly increased due to several factors, such as the duration of heating, the type of tissue involved, and patient-specific characteristics, including age and general physical condition [34]. This behaviour introduces additional uncertainty, and, in order to model perfusion enhancement, ESHO recommends the use of a static thermal stress model, neglecting transient variations of blood perfusion during the computations [1]. The thermal properties of the tumor were assumed to be identical to those of muscle, with the exception of the perfusion rate. Moreover, the thermal model needs to be completed by an initial temperature condition $T = T_{\text{in}}$ at the initial time $t = t_{\text{on}}$ and by proper boundary conditions, which describe the thermal interaction of the system with the surrounding environment [4]:

$$\hat{\mathbf{n}} \cdot (k\nabla T) = h\,(T_{\text{ext}} - T) \tag{2.1}$$

where $\hat{\mathbf{n}}$ is the unit vector normal to the considered boundary, h (W/(m^2 °C)) is the heat transfer coefficient, and T_{ext} (°C) is the external reference temperature.

ESHO has also provided specific guidelines on how thermal simulations should be performed, followed in this work and summarized below [1]:

- Patient's initial temperature set to $T_{\text{in}} = 37$°C.
- Convective boundary conditions for waterbolus surface and external air temperature fixed at $T_{\text{ext}} = 20$°C.
- Heat transfer coefficients of $h = 6$ W/(m^2 °C) and of $h = 40$ W/(m^2 °C) at the interface to, respectively, the external air and waterbolus.
- Two possible options can be considered for modeling the internal air: either including it in the computational domain and increasing its specific heat capacity (1004 J/Kg $\cdot$ C) by a factor of 10, or excluding it from the computational domain and applying a convective boundary condition at the corresponding interfaces.

In our case, the internal air was included in the computational domain and modelled with a specific heat capacity of 10 040 J/(kg · °C), since this does not affect steady-state temperatures.

As for the computational grid, the same maximum step of 2.5 mm was applied to the patient tissues, the water bolus and the VOI sensor, whereas the antennas and the surrounding background were excluded from the computational domain. This resulted in a final grid of approximately 6.32 million cells.

2.3 Optimization Benchmark

As mentioned in Section 1.4, two main classes of optimization strategies can be distinguished: SAR-based optimization and temperature-based optimization. In clinical practice, among the most advanced approaches both the SAR-based optimization (e.g. in VEDO [35]) and the temperature-based optimization (e.g. in Plan2Heat [36]) are currently used in the clinical setting. For the Alex head and neck model, ESHO [1] adopted a temperature-based optimization strategy, whose objective is to achieve a homogeneous target temperature T_{goal} within the HTV by minimizing an objective function θ:

$$\theta = \int \Big(T_{\text{goal}} - T(x) \Big)^2 \, dx \tag{2.2}$$

where $x \in \text{HTV}$ and $T(x) < T_{\text{goal}}$. In this specific case T_{goal} was set to 43 °C and hard constraints of 44 °C were applied to both normal tissues and tumor to avoid thermal injuries and reduce risk for the patient.

In addition to the Alex model, the associated dataset containing several parameters was provided. This dataset has been fundamental for achieving our goal of reproducing the benchmark results. It consisted of essential quantities such as vectors collecting the dielectric and thermal properties of all tissues, several clinical evaluation parameters such as T10, T50 and T90 (temperatures achieved in at least 10%, 50% and 90% of the HTV, respectively), and the temperature-optimized feeding coefficients for antenna amplitudes and phases. The latter are reported in the Table 2.4, where the twelve ports of the applicator are indexed as $L_{01} \dots L_{06}$ and $R_{01} \dots R_{06}$.

Table 2.4: Temperature-optimized excitation amplitudes and phases for each port, as reported in the ESHO Dataset.

Antenna	Index	Amplitude (W)	Phase (°)
L_{01}	1	9.229	0.00
L_{02}	2	8.132	97.24
L_{03}	3	14.301	47.98
L_{04}	4	3.808	174.57
L_{05}	5	2.751	32.99
L_{06}	6	3.621	-71.77
R_{01}	7	6.747	-24.07
R_{02}	8	9.369	85.94
R_{03}	9	12.473	87.87
R_{04}	10	5.794	168.70
R_{05}	11	5.231	76.01
R_{06}	12	2.735	13.90

2.4 SAR and Temperature Distributions

After performing the EM Multiport simulation (and subsequently using the PLD as the source term for the thermal simulations), it was necessary to define an input power for the antennas. In this context, the guideline proposed by ESHO - although not prescribing a specific power level— recommends increasing input power until a maximum temperature of 44°C is achieved in both tumor and normal tissues [1]. In order to achieve this, several input power values were analyzed using the Simulation Combiner tool, testing values within the range 1–350 W. The aim was to identify the input power value that was most likely adopted in the original ESHO study, or at least the one that best reproduced their reported SAR and temperature distributions, shown in Figure 2.5.

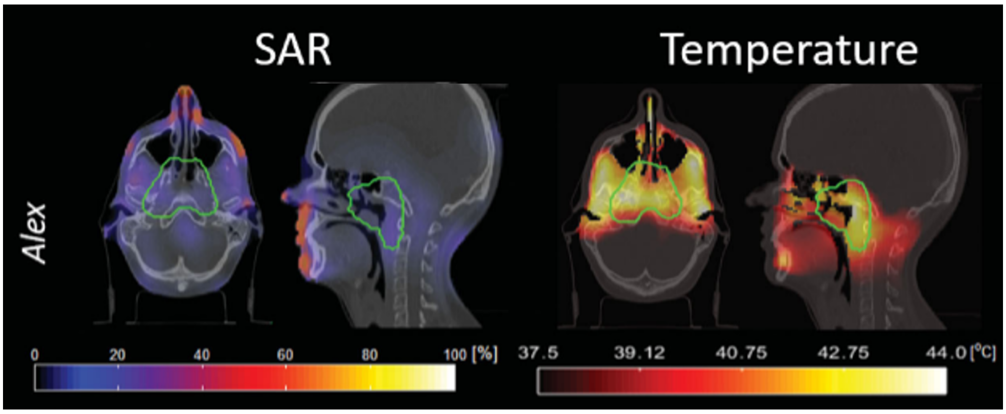

Figure 2.5: Axial and sagittal cross-sections of the optimized SAR and Temperature maps in the ESHO model Alex. Target region indicated by green contour [1].

It is important to note that the extraction domain was restricted to the region of interest by excluding entities not relevant to the analysis. This was achieved using Sim4Life's Mask Filter tool, which masks 3D fields by assigning zero (or a defined replacement value) to voxels outside the selected region. The background, water bolus, and antennas were excluded, leaving only the tumor and healthy tissue voxels. Subsequently, the extraction was further refined to the VOI sensor corresponding to the Alex H&N region (see Section 2.2.2). The resulting data were exported via the MATLAB Exporter, reshaped in MATLAB, and visualized on central slices passing through the tumor in the axial (xy) and sagittal (yz) planes.

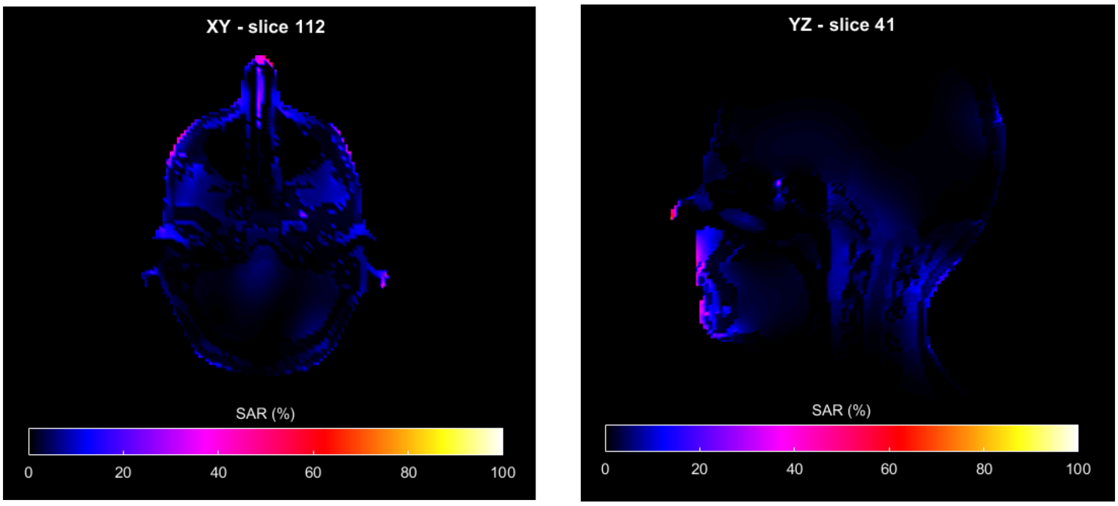

Figure 2.6: Normalized SAR distributions obtained using ESHO's temperature-optimized antenna excitations with a 300 W total input power.

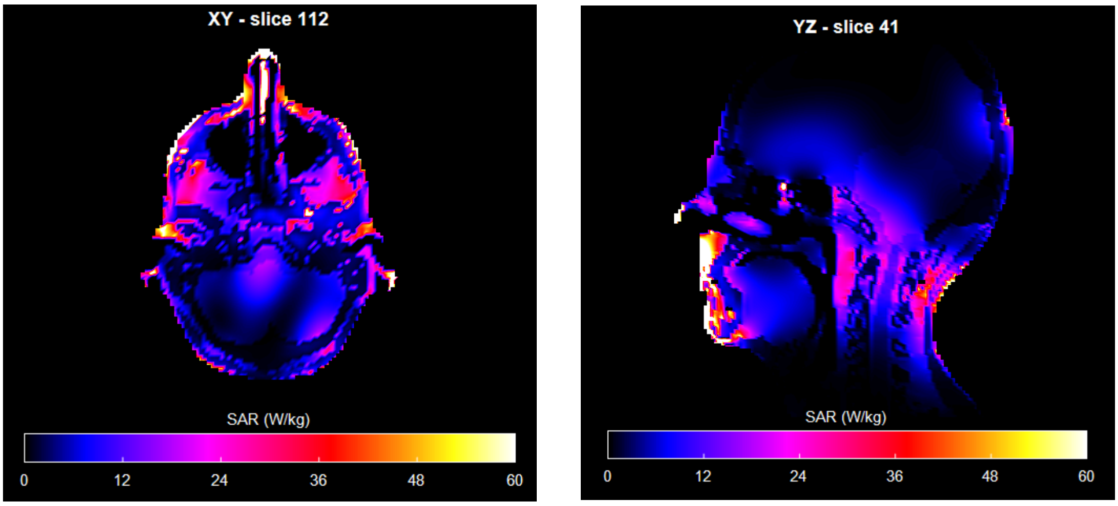

Figure 2.7: Absolute SAR distributions obtained using ESHO's temperature-optimized antenna excitations with a 300 W total input power.

The SAR maps obtained with a normalized input power of 300 W, using the temperature-optimized excitation coefficients (Table 2.4), are shown in Figure 2.6. The resulting SAR distribution closely resembles the ESHO benchmark, particularly within the main focusing regions (Figure 2.5).
For completeness and improved readability, the corresponding absolute-scale SAR maps are provided in Figure 2.7, where the similarity with ESHO is even more apparent. Clear hotspots appear in the nose, mouth, and chin regions. Within the tumor, the pattern exhibits moderate focusing without localized absorption peaks. This behavior is consistent with temperature-based optimization, which reduces the weighting of small-volume hotspots—as long as they remain below specified thresholds—while emphasizing the average performance within the HTV [1].

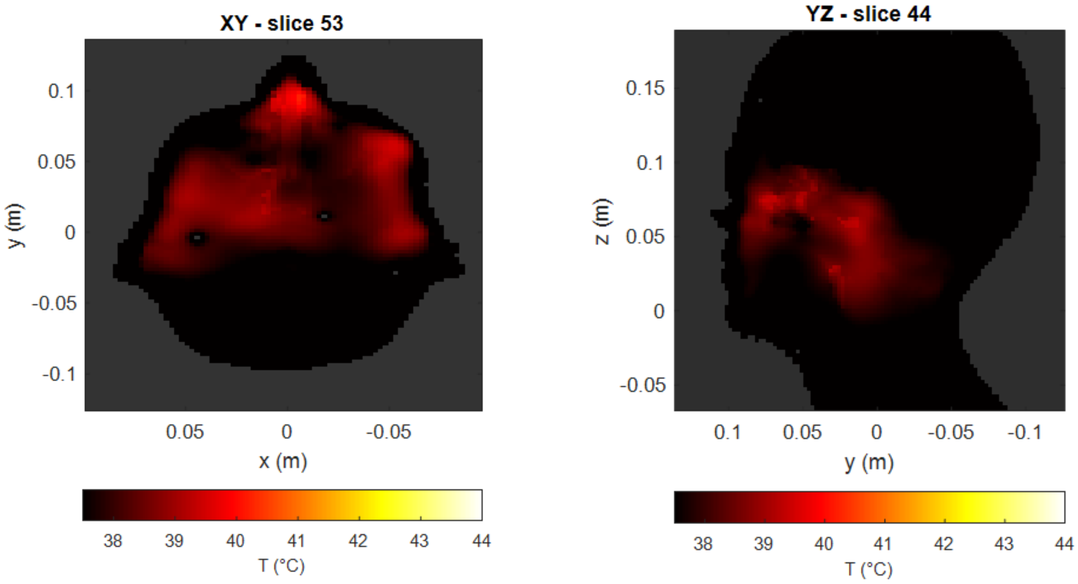

Figure 2.8: Temperature distributions obtained using ESHO's temperature-optimized antenna excitations with a 300 W total input power.

The corresponding temperature distributions derived from the 300 W SAR maps (Figure 2.7) are shown in Figure 2.8. Axial and sagittal sections indicate that, despite an input power of 300 W, the temperature profiles do not reproduce those reported by ESHO (Figure 2.5). The focusing is overall satisfactory—no hazardous hot spots are visible in the surrounding healthy tissues, and sensitive structures such as the brain and eyes do not exhibit temperature rises—yet the temperatures within the target region remain below the desired clinical levels. These results suggest that the 300 W input power is insufficient to reproduce the ESHO benchmark. Therefore, the input power was increased to 500 W, with the resulting temperature maps shown in Figure 2.9.

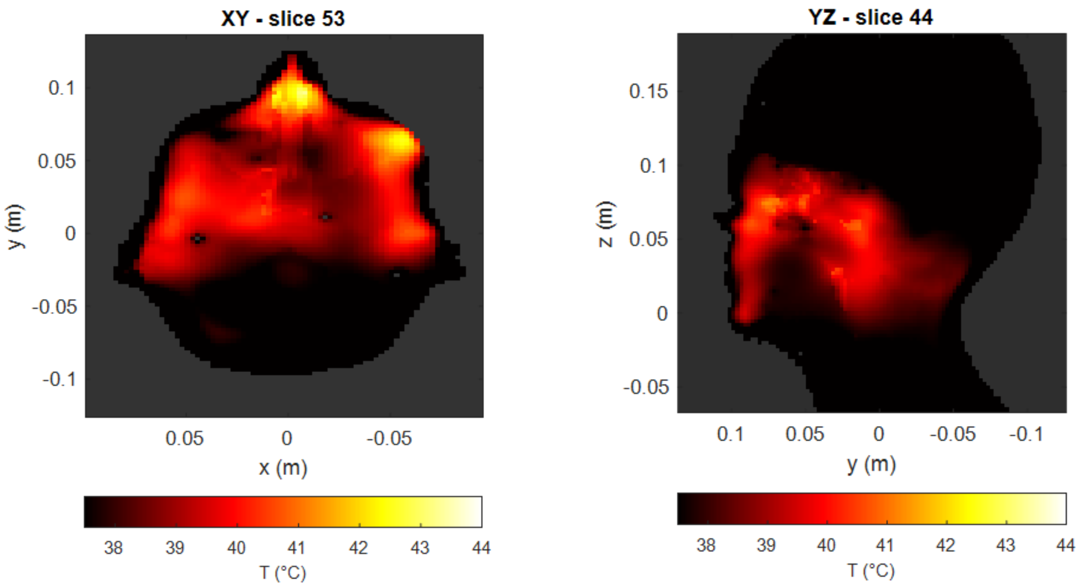

Figure 2.9: Temperature distributions obtained using ESHO's temperature-optimized antenna excitations with a 500 W total input power.

The ESHO benchmark states that "a T50 of more than 40 °C is generally considered sufficient for treatment, but treatment effect is expected to increase when temperatures are closer to 43 °C ". Compared with the 300 W case, the 500 W configuration yields temperature distribution much closer to this clinical target, albeit at the cost of increased power consumption. This finding suggests that temperature-based optimization, as adopted by ESHO, may be less power-efficient in this setting. In contrast, SAR-based optimization techniques [5] enable better focusing and improved thermal efficiency at lower power levels, as will be discussed in Section 3.1.

Chapter 3

Temperature Reconstruction

This chapter presents the recently proposed temperature-reconstruction approach, which delivers real-time 3D temperature information from a limited set of measurement points. We begin with the SAR-based optimization, then outline the key stages of the Temperature Reconstruction workflow [4], from defining relevant tissues and the parameter space to multigrid construction and temperature-map extraction. These maps provide then the inputs required for the correct application of the reconstruction process.

3.1 SAR-Based Optimization

As discussed in Section 1.4, optimization strategies can be broadly classified into temperature-based and SAR-based approaches. Owing to their higher efficiency and lower computational cost, SAR-based methods are typically preferred, and this thesis adopts that choice. Specifically, we employed Particle Swarm Optimization (PSO), an algorithm inspired by the social behavior of birds and fish, in which a "swarm" of particles - candidate solutions - explores the solution space by updating their positions according to both individual and collective best performances [37]. From a mathematical standpoint, the SAR optimization method can be formalized as follows [5], starting from the definition of the SAR (1.7) introduced in Section 1.3.1. In that equation, the total electric field $\mathbf{E}(\mathbf{r})$ can be expressed as a superposition of the electric fields generated by each antenna acting independently and the unknown excitation coefficient:

$$\boldsymbol{E}(\boldsymbol{r}) = \sum_{n=1}^{N} \tilde{v}_n \, \boldsymbol{e_n}(\boldsymbol{r}) \tag{3.1}$$

In this equation $\boldsymbol{e_n}(\boldsymbol{r})$ is the field generated by the n-th antenna when fed by unitary excitation, and $\tilde{\nu}_n$ is the n-th antenna excitation coefficient—considering both amplitude and phase—as part of the array, which can be expressed as follows:

$$\tilde{\nu}_n = \nu_0 \cdot \xi_n \cdot e^{i\varphi_n}, \tag{3.2}$$

where $\nu_0 = \dfrac{\sqrt{2R_0P_0}}{\|\boldsymbol{\xi}\|^2}$ is a constant amplitude coefficient, with $R_0 = 50\,\Omega$ and P_0 the total power delivered to the array, while $\xi_n \in [0,1]$ denotes the normalized amplitude coefficient and $\varphi_n \in [0,2\pi)$ represents the phase.

In each SAR-based optimization, the primary goal is to maximize power deposition within the tumor region while minimizing the risk of overheating in the surrounding healthy tissues. This, in turn, requires minimizing the Hotspot-to-Target Quotient (HTQ), defined as:

$$\mathrm{HTQ} = \frac{\langle \mathrm{SAR}_{V_1} \rangle}{\langle \mathrm{SAR}_{\mathrm{target}} \rangle} \tag{3.3}$$

where $\langle \mathrm{SAR}_{V_1} \rangle$ is the average SAR in V_1, with V_1 equal to the 1% of the healthy volume with the highest SAR, and $\langle \mathrm{SAR}_{\mathrm{target}} \rangle$ the average SAR in the target region.

In our specific case, to implement PSO we extracted the stand-alone fields — i.e., the fields obtained by each antenna individually while all others are switched off — using a dedicated Python script. These fields were computed voxel by voxel and stored in .mat files in order to be then imported into MATLAB, where the PSO algorithm was executed to determine the optimal set of feeding coefficients (amplitude and phase) for the antenna array. These coefficients are listed in Table 3.1 and are employed throughout all the remaining simulations and tests performed in this study.

After computing the coefficients, the Simulation Combiner tool was used again to test the effectiveness of the implemented optimization. Resulting SAR fields and temperature distributions obtained with the new coefficients are reported, keeping the normalized input power at 300 W to enable a fair comparison.

As shown in Figure 3.1, the SAR focusing is markedly improved compared with the temperature-based optimization (Figure 2.7): the radiation is concentrated on the target, and the majority of peaks are now closer to the tumor volume. Moreover, the hot spots originally observed in the nasal and oral regions disappeared, while the chin hot spot has been substantially reduced.

The temperature distribution (Figure 3.2) likewise shows clear improvements: the temperature rise is further confined to the target region, healthy tissues are preserved, and higher intratumoral peaks are achieved within the GTV. Overall, the implemented SAR-based optimization can be considered successful: it removes

Table 3.1: Amplitudes and phases for each port obtained with the SAR-based PSO approach.

Antenna	Index n	Amplitude ξ_n (-)	Phase φ_n (°)
L_{01}	1	$9.508e{-9}$	2.34
L_{02}	2	0.2169	289.07
L_{03}	3	0.994	41.16
L_{04}	4	0.214	360
L_{05}	5	0.005	123.86
L_{06}	6	0.339	61.94
R_{01}	7	$4.269e{-13}$	0.01
R_{02}	8	0.187	0
R_{03}	9	0.929	353.16
R_{04}	10	0.178	10.21
R_{05}	11	0.010	242.26
R_{06}	12	0.105	360

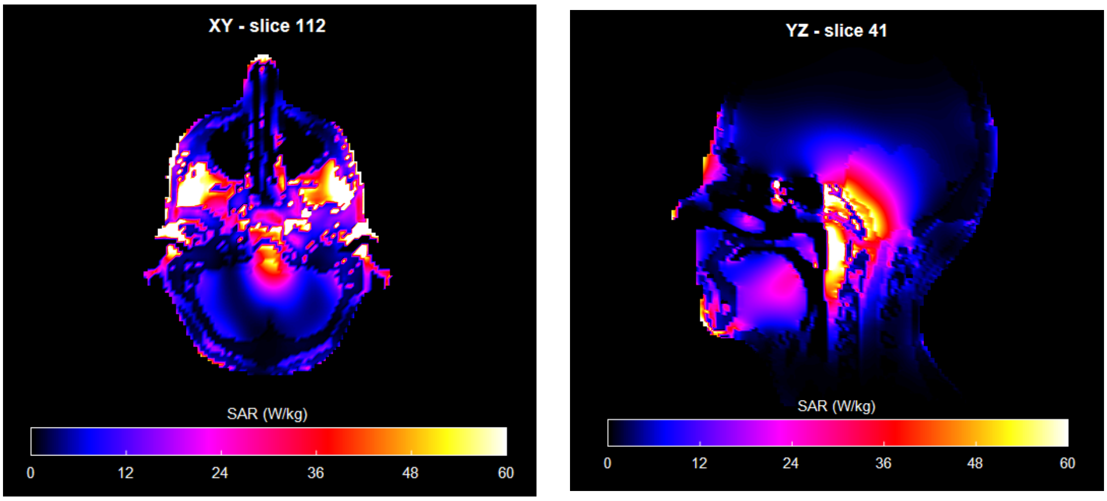

Figure 3.1: Absolute SAR distributions obtained using SAR-based optimized (PSO) antenna excitations with a 300 W total input power.

pre-existing hot spots while preventing new internal ones, reduces energy deposition in non-treated tissues, and increases the maximum temperature reached in the target area.

It is necessary to specify that to comply with the ESHO safety criterion—input power should be scaled so that temperatures in both tumor and normal tissues

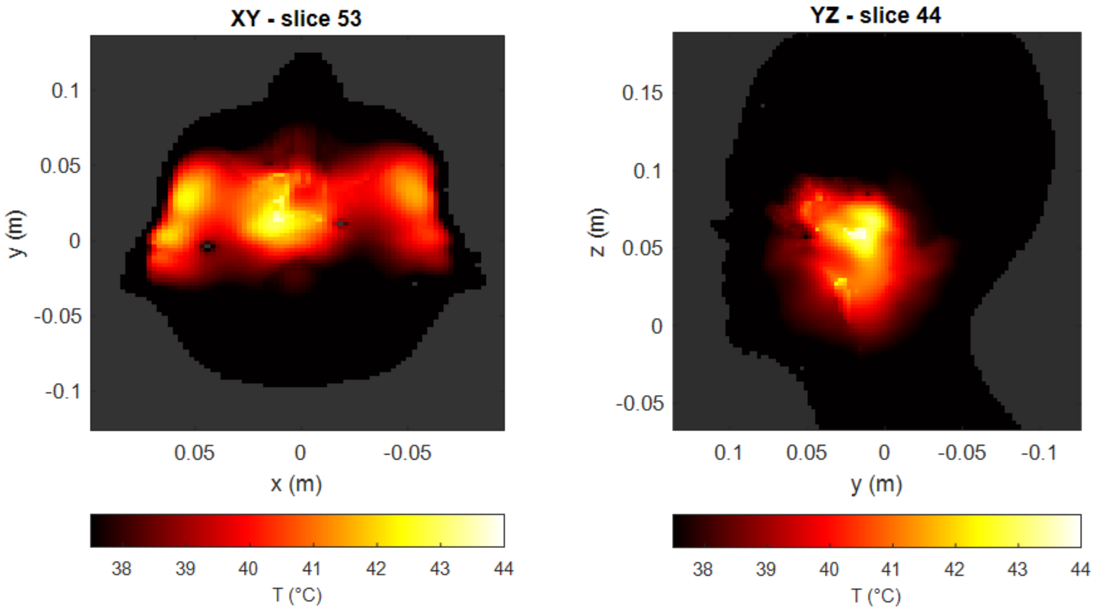

Figure 3.2: Temperature distributions obtained using SAR-based optimized (PSO) antenna excitations with a 290 W total input power.

do not exceed 44 °C [1]—we slightly reduced the applied power. At 300 W, the threshold was exceeded by a small margin (see Table 3.2); lowering the input to 290 W restored compliance while still yielding satisfactory heating in the target region, as confirmed by the T50 and maximum temperature values observed in the GTV, HTV and for healthy tissues. For this reason, the distribution obtained with this input power, $\mathbf{s}_{\text{base}}$ parameters - dielectric and thermal parameters' set introduced in Section 2.2.1 - and the feeding coefficients obtained through the SAR-based optimization will be regarded, from this point onward, as the baseline map for the subsequent analysis.

Table 3.2: Temperature metrics for GTV, HTV and healthy tissues obtained with SAR-Based optimization. Both the efficiency condition — T50 above 40 °C — and the safety condition — temperature not exceeding 44 °C in all tissue types — proposed by ESHO [1] are satisfied with 290W as input power.

	GTV				**HTV**				**Healthy tissues**
Input Power	T90	T50	T10	Tmax	T90	T50	T10	Tmax	Tmax
300W	39,56	41,39	42,88	43,61	38,85	40,48	42,14	44,20	44,04
290W	39,47	41,24	42,69	43,39	38,79	40,36	41,97	43,96	43,75

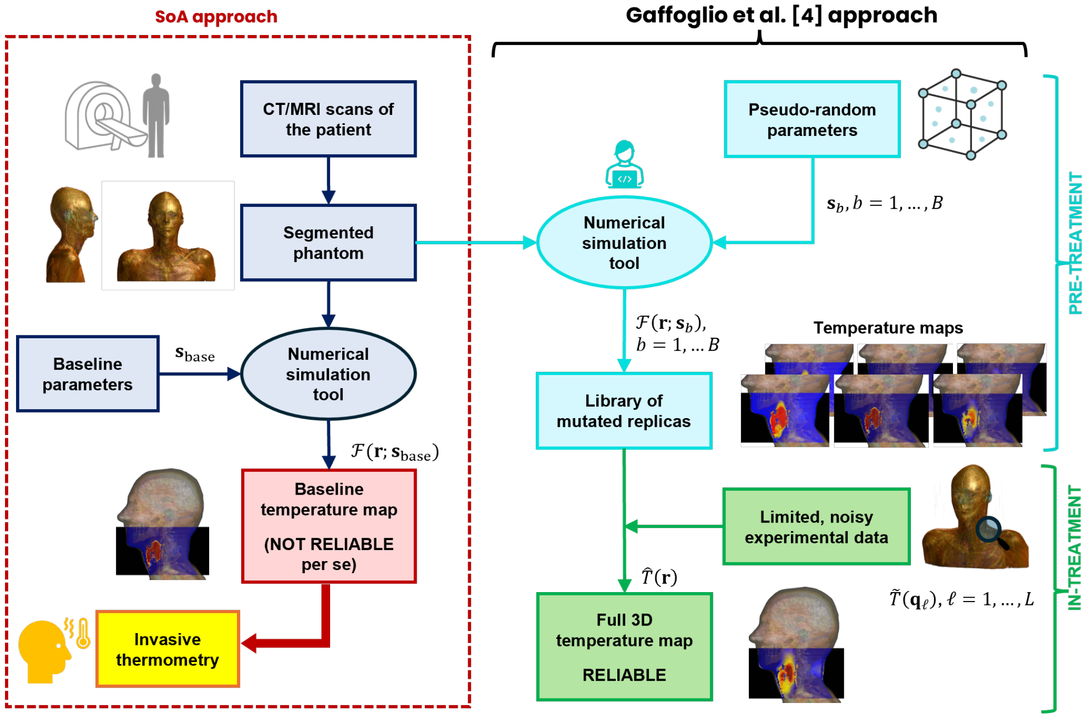

Figure 3.3: Flow chart reporting the state of art (SoA) approach and Gaffoglio et al. reconstruction method [4]. The scheme illustrates how the reconstruction method leverages a set of patient-specific simulations obtained by varying the constituent parameters during the pre-treatment stage. The elements of this simulation set are then combined with the limited experimental data acquired during treatment, ultimately providing a reliable real-time temperature map of the ROI.

3.2 Reconstruction Method Workflow

The approach described in this section consists in creating a patient specific set of temperature simulations in the ROI - corresponding to different combinations of the constituent parameters - and then match this set to limited data acquired during the treatment to obtain, in real time, a realistic 3D temperature map of the patient [4].
Once the SAR-based optimization is finalized - and the set of optimal feeding coefficients has been selected - the reconstruction process can begin.

As shown in the Figure 3.3, the initial stages of this approach—patient image acquisition and phantom segmentation—were already introduced in Section 1.4. The resulting patient model is then imported, together with the HT applicator, into a simulation environment—Sim4Life in our case—that solves Maxwell's equations

and the PBHE (Section 2.2). Simulations are here performed assigning to phantom's tissues the baseline set of dielectric and thermal properties i.e. $\mathbf{s}_{\text{base}}$.
From this point onward, the reconstruction method departs from the state-of-the-art (SoA) approach (Figure 3.3). The simulated temperature map $\mathcal{F}\Big(\mathbf{r};\, \mathbf{s}_{\text{base}}\Big)$, with $\mathbf{r}$ belonging to the mesh points in the ROI, is not reliable per se, owing to the high uncertainty that particularly affects thermal parameters under thermal stress. This typically necessitates invasive thermometry, which, as discussed in Section 1.5.2, provides only limited temperature control.
To address this, the reconstruction method strengthens the pre-treatment phase, beginning with a careful analysis of tissue properties: first identifying the relevant tissues, then defining the parameter space. Subsequently, a multigrid of parameter combinations is generated by mutating the constituent parameters $\mathbf{s}_b,\ b = 1, \dots, B$, within literature-derived variation ranges. This set is used to build a patient-specific library of temperature maps that reproduce the heating process within the ROI. After extracting these mutated replicas, a small number of measurement points $\tilde{T}(\mathbf{q}_\ell),\ \ell = 1, \dots, L$, is acquired during treatment. Finally, by combining elements from the library in the way that best matches the limited measurement data, a real-time 3D temperature map of the ROI can be obtained [4].

3.2.1 Relevant Tissues

Before presenting the temperature reconstruction methodology, a preliminary analysis of the region of interest - our model's VOI - was carried out to determine which tissues are predominantly represented within it. To this end, the vector of dielectric conductivities of healthy tissues in the VOI, i.e. σ_H, was exported from Sim4Life and examined in MATLAB to identify the set of relevant tissues for subsequent analysis.

To formalize this, we define:

- t_i: the i-th tissue;
- σ_i: the dielectric conductivity of the i-th tissue;
- N_i: the number of sampling points with conductivity σ_i;
- $N_{\text{tot}} = \sum_i N_i$: the total number of sampling points in σ_H.

The percentage presence of tissue t_i is then computed as

$$r_i(\%) = 100\, \frac{N_i}{N_{\text{tot}}},$$

which quantifies the fraction of points in σ_H corresponding to conductivity σ_i and thus the relative presence of tissue t_i within the VOI. The results are displayed as a histogram (Figure 3.4).

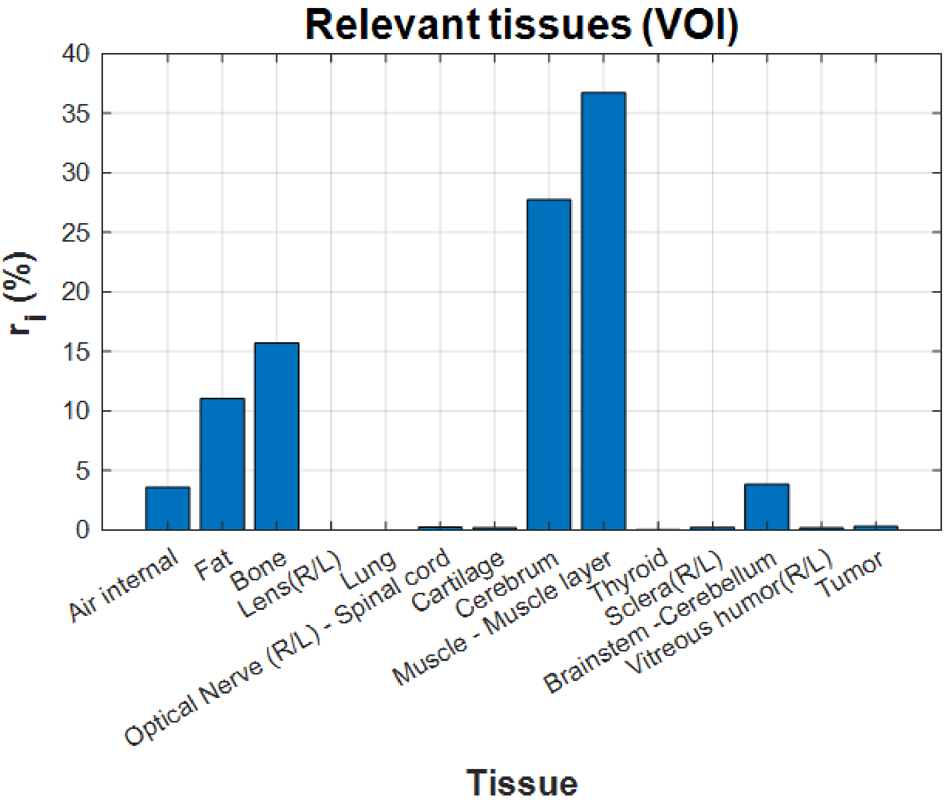

Figure 3.4: Percentage composition of tissues within the VOI, computed from the conductivity vector σ_H . Muscle, cerebrum, and fat dominate the region of interest; bone is not considered further because of its comparatively well constrained thermal properties.

The histogram shows that the tissues most represented in the VOI are muscle, cerebrum, bone, and fat. However, since bone exhibits poor conductivity and substantially lower uncertainty in thermal properties than the other tissues [38], it was excluded from further analysis. Consequently, the parameter space examined in the next section (3.2.2) focuses on muscle, cerebrum, and fat; the tumor is retained as a dedicated class—irrespective of its relatively modest volume fraction in the VOI - $r(\%) = 0.327$ — since it is the target of the treatment and presents considerable thermal uncertainty.

While the high prevalence of muscle and fat within the VOI is expected, Figure 3.5 is provided to emphasize the relevance of cerebrum due to its anatomical proximity to the tumor and its pronounced thermosensitivity [12].

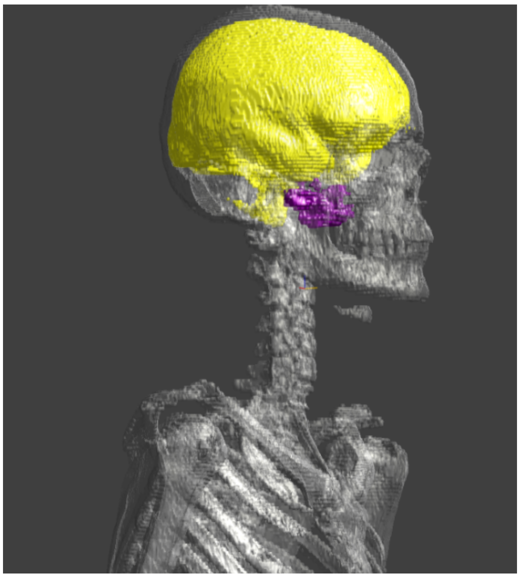

Figure 3.5: Alex model side view, only Bones (white), GTV (purple) and Cerebrum (yellow) are displayed.

3.2.2 Parameters Space and Multigrid Creation

After identifying the relevant tissues (muscle, cerebrum, fat, and tumor), we define the parameters space by specifying the variation ranges for the thermal properties—thermal conductivity k and blood perfusion ω. In particular, ω is subject to substantial uncertainty; adopting suitably broad ranges for these parameters enables the method to handle their variability even under thermal stress [4]. The values used in this work are reported in Table 3.3.

Table 3.3: Considered tissues' properties, baseline values, and range of variation

	k (W/(m°C))			ω (ml/(min kg))		
Tissue	Baseline	min	max	Baseline	min	max
Muscle	0.49	0.40[a]	0.56[a]	188.7	19[a]	442.8[a]
Fat	0.21	0.18[a]	0.50[a]	69	20[a]	255[a]
Cerebrum	0.55	0.53[b]	0.56[b]	763.3	671[b]	840[b]
Tumor	0.49	0.41[a]	1.50[a]	94.4	36.15[a]	848[a]

The baseline values are derived from the ESHO benchmarck database [1]. **a**: values as used in [4]; **b**: values derived from the IT'IS database [31].

The baseline values are drawn from the ESHO benchmark [1], as introduced in Section 2.2.1. For the minimum and maximum bounds, we distinguish by tissue: for the cerebrum, variability ranges are taken from the IT'IS database [31], whereas for muscle, fat, and tumor the lower and upper limits are those identified in [4].

The parameter space is N-dimensional, where N equals the number of tissues multiplied by the number of parameters. In this thesis, selecting two thermal parameters—thermal conductivity k and perfusion ω —for four tissues (muscle, cerebrum, fat, and tumor) yields an 8-dimensional space. Each configuration corresponds to a point having a unique set of 8 coordinates, within an 8-D hypercube whose sides are bounded by the minimum and maximum values reported in Table 3.3.

The parameter space is discretized into a multigrid, a set of N-tuples, each specifying one combination across the selected parameters and tissues. In this work, Sobol sampling is used to generate 256 variations of k and ω for the relevant tissues. The grid is produced in MATLAB with the MultiGrid_Sobol_B function, with the possibility to add the baseline case as first point via the "_baseline" variant. The resulting matrix is saved to a text file and subsequently used to build the library of temperature maps. The Sobol sequence is a low-discrepancy design that provides more space-filling, uniformly spread samples than purely random (Monte Carlo) draws, including a higher uniformity [4]. This reduces gaps and clustering tendencies and yields a more balanced coverage of the 8-D hypercube.

3.2.3 Temperature Maps Extraction

Once the matrix of parameter variations for k and ω (for the selected tissues) has been generated and saved as a `.txt` file, we proceed to build the library of temperature maps. These maps can be computed pre-treatment and represent the possible outcomes of the simulation for the same patient.

For the extraction, the Python script `Basis_maps_extraction_w_k.py` is executed in the Sim4Life Scripter, iterating over the N-tuples contained in `MGrid.txt`— $N = 256$ in our case (see previous subsection)—and computing the corresponding temperature fields. Each temperature map is obtained by solving the steady-state bioheat equation after assigning a specific set of values $\boldsymbol{\xi}$ to the variable parameters of the relevant tissues, while all other tissue properties are set to their baseline values [1, 4]. Each run saves a temperature map to the designated `T_maps` folder; repeating the procedure with updated multigrids yields the complete basis set of temperature maps. Subsequently, in MATLAB, using Phi_Basis.m code, these maps are assembled into the basis matrix ϕ, with ROI points (after NaN removal) as rows and parameter-combination instances as columns.

From the assembled basis matrix ϕ, we also extract target maps—simulated temperature fields corresponding to specific parameter combinations—used to test the reconstruction method.

In Figure 3.6, a random subset of the 256 extracted maps is shown. The observed differences in temperature distributions illustrate that variations in the thermal parameters - even of a small set of selected tissues - can yield markedly different thermal profiles.

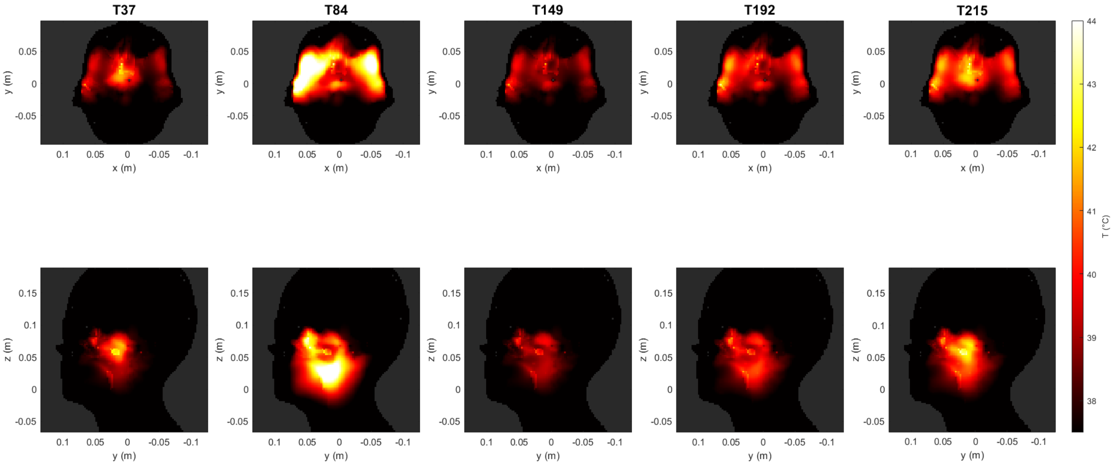

Figure 3.6: Random maps extracted from the built library

3.3 Reconstruction Process

After identifying the relevant tissues, defining the variation ranges of the thermal parameters, and simulating/extracting the corresponding temperature fields, the reconstruction method can be applied. As introduced earlier, this approach is designed to recover real-time 3D temperature information in the patient's ROI from a small number of noisy measurement points, leveraging simulations performed pre-treatment. To this end, it integrates two information sources: (i) a library of steady-state thermal simulations that accounts for uncertainty arising from variability in tissue properties (see Section 3.2.3), and (ii) temperature measurements acquired by sensors, which are unavoidably affected by noise [4].

Reconstruction method used in this thesis can be analyzed from mathematical point of view as described in [4]. With $T(\mathbf{r}, t)$ is indicated the temperature distribution at the spatial point $\mathbf{r}$ solving the steady–state version of the bioheat equation in the ROI. Given L temperature values $\tilde{T}(\mathbf{q}_\ell)$, acquired in $\mathbf{q}_\ell$, $\ell = 1, \dots, L$ - points along a specific direction in the ROI, mimicking the acquisition points of a fiber optic thermometer - and inherently affected by measurement uncertainties, the goal is to approximate the temperature distribution $\widehat{T}(\mathbf{r})$ in the whole ROI as a finite superposition of B reconstruction functions ϕ_b, i.e.:

$$\widehat{T}(\mathbf{r}) = \sum_{b=1}^{B} \mathrm{w}_b \, \phi_b(\mathbf{r}), \tag{3.4}$$

where w_b are the corresponding weights. The reconstruction functions $\phi_b(\mathbf{r})$ used in Eq. (3.4) are temperature distributions obtained with multiphysics simulations where a set of constituent parameters is assigned to the model.
Indicating with the N-tuple $\mathbf{s}_b$ the set of values assigned to the N relevant parameters used in the simulation solver, the reconstruction function ϕ_b in Eq. (3.4) can be written as $\mathcal{F}(\mathbf{r}; \mathbf{s}_b)$, where $\mathbf{r}$ belongs to the set of mesh points in the simulated ROI.

Inversion Algorithm:

Since the goal is to reconstruct a volumetric temperature distribution from sparse and noisy line measurements, the resulting inverse problem is ill-posed, necessitating the use of regularization to ensure stability and reliability [4]. The regularization approach employed in this thesis is the constrained least squares (CLS) method, which is expressed by:

$$\min_{\mathrm{w} \in \mathbb{R}^B} \sum_{\ell=1}^{L} \left(\sum_{b=1}^{B} \mathrm{w}_b \, \mathcal{F}(\mathbf{q}_\ell; \mathbf{s}_b) - \tilde{T}(\mathbf{q}_\ell) \right)^2 . \tag{3.5}$$

with the additional constraints:

$$\sum_{b=1}^{B} \mathrm{w}_b = 1, \qquad \mathrm{w}_b \geq 0 \quad \forall \, b = 1, \ldots, B. \tag{3.6}$$

The weights w_b are determined by minimizing the discrepancy between the measured data points $\tilde{T}(\mathbf{q}_\ell)$, $\ell = 1, \ldots, L$, and the approximation in (3.4) evaluated at the same spatial positions, namely $\hat{T}(\mathbf{q}_\ell)$. In this work, CLS problem is solved using the MATLAB routine lsqlin, that recasts the problem as a quadratic one with linear constraints and uses an interior-point method to solve it.

The temperature values $\mathcal{F}(\mathbf{q}_\ell; \mathbf{s}_b)$, $b = 1, \ldots, B$, in Eq. (3.5) are evaluated by solving the steady–state version of the bioheat equation in the ROI for B combinations $\mathbf{s}_b$ of the selected set of parameters. In our work, two thermal parameters have been varied for four tissues in the ROI (Section 3.2.2) for a total of 8 parameters, while B has been imposed equal to 70 since, for this value, adding additional reconstruction functions does not produce significant changes in the reconstructed map [4]. Regarding L temperature values used, they are obtained from target maps $\mathcal{F}(\mathbf{r}; \boldsymbol{\xi}_a)$, where $\boldsymbol{\xi}_a$, $a \in \{1, \ldots, A\}$, are combinations of the selected constituent parameters, corresponding to sequence elements different from the sets $\mathbf{s}_b$, $b \in \{1, \dots, B\}$.

Noise:

To account for measurement noise throughout the process, Gaussian noise has been added to the temperature values used in the reconstruction, expressed as:

$$\tilde{T}(\mathbf{q}_\ell) = \mathcal{F}(\mathbf{q}_\ell; \boldsymbol{\xi}_a) + f_{\mathcal{N}}(\mathbf{q}_\ell; \mu, \sigma^2). \tag{3.7}$$

In this thesis, we decided to use 1000 realizations of Gaussian error and respectively set the standard deviation to $\sigma = 0.2°\text{C}$ and the mean systematic noise to $\mu = \pm 0.1°\text{C}$.

Evaluation Metrics:

The accuracy of the obtained results is assessed by computing the median of the absolute temperature differences ΔT between the target map and the reconstructed temperature distribution $\widehat{T}(\mathbf{r})$. To quantify the results, the following goodness function $g(\chi)$ is introduced [4]:

$$g(\chi) = \frac{\mathrm{Vol}\Big(\{\, \boldsymbol{r} \in \mathrm{ROI} : |\Delta T(\boldsymbol{r})| \leq \chi \,\}\Big)}{\mathrm{Vol}(\mathrm{ROI})}. \tag{3.8}$$

The goodness function represents the relative size of the region where the absolute temperature difference ΔT is below a given threshold χ (°C). In the case that $g(\chi) = 1$ for all χ, a perfect reconstruction has been obtained [4].

Chapter 4

Results

This chapter outlines results obtained with the application of the temperature reconstruction method, testing its performance for a number of realistic catheter configurations. The cases essentially differ from each other in terms of catheter position and orientation, insertion path, and number of measurement points acquired along the fiber-optic thermometer. For each configuration, the corresponding setup is described and the resulting reconstructions are evaluated in terms of goodness function values and temperature errors.

4.1 Catheter Cases

To perform the analysis, temperature reconstruction was carried out using a single catheter, tested in seven different configurations. The main geometric and sampling parameters of each configuration are summarized in Table 4.1. Depending on the chosen parameters, the catheter trajectories are more or less invasive: some of them reach the tumor region, whereas others remain outside it, and they also feature different sampling patterns of the fiber-optic thermometer.

The parameters that define and distinguish the different catheter placements are the following:

Type**:** catheter type, x or y. An x-type catheter lies along the line $y = y_c$, whereas a y-type catheter lies along the line $x = x_c$.

Coordinate **(mm):** the value of x_c or y_c specifying the catheter position in the transverse plane.

Direction**:** once the catheter position is fixed, this parameter describes the direction along which the measurement points are sampled with respect to the phantom. With *fw* (forward) the points are collected starting from one endpoint of the line and moving inward, whereas *rev* (reverse) starts from the opposite endpoint.

$\mathbf{N}_{\text{cath}}$: number of measurement points (sensors) considered along the catheter.

***Spacing* (mm):** distance between adjacent measurement points along the catheter.

The different configurations are visualized in the xy-plane; therefore, for each case a value of z_c is also specified to identify the catheter position along the z-axis. In this study, the same value $z_c = 62\,\text{mm}$ was used for all configurations, since this coordinate corresponds to the xy-slice passing through the tumor centroid. All catheter configurations tested are displayed in Figure 4.1.

Table 4.1: Catheter configuration parameters.

Case	Type	Coordinate (mm)	N_{cath}	Direction	Spacing (mm)
1	y	-0.6	20	rev	2.5
2	x	21.2	7	rev	7.5
3	y	18.8	10	rev	5
4	x	21.2	13	fw	5
5	y	-20.8	10	rev	5
6	x	21.2	10	rev	5
7	y	-0.6	11	fw	10

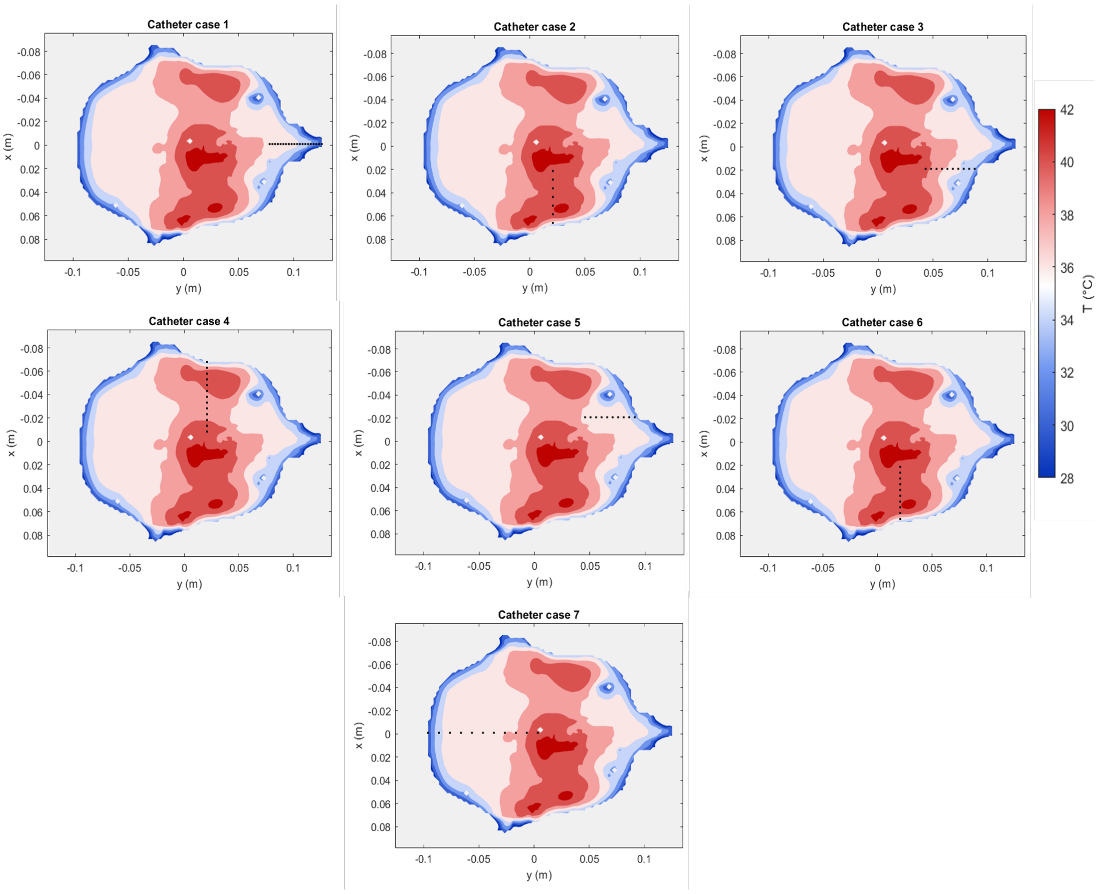
Catheter case 1

Catheter case 2

Catheter case 3

Catheter case 4

Catheter case 5

Catheter case 6

Catheter case 7

Figure 4.1: Catheter cases employed in this work. The seven catheter trajectories are displayed on the transverse *xy*-plane at $z_c = 62$ mm. Depending on the chosen parameters (type, coordinate, number of sensors and direction), the catheter paths are located at different distances from the tumor region, resulting in configurations that are more or less close to the heated target. All cases correspond to relatively invasive trajectories, with the exception of Case 1, which follows a less invasive path through the nasal cavity.

4.2 Reconstruction Error

The quality of the reconstructed temperature distributions was assessed by analyzing the behavior of the goodness function introduced in Section 3.3 and by computing error metrics between the reconstructed and target temperatures. For each catheter case, the evolution of the goodness function is reported.

In order to perform this analysis, 70 maps among the 256 extracted in Section 3.2.3 have been used as reconstruction functions, while some of the remaining maps have been treated as target maps. The target maps correspond to simulated temperature distributions obtained for a specific combination of the constituent parameters. Indicating with $\mathcal{F}(\mathbf{r};\boldsymbol{\xi}_a)$ a target temperature map obtained by solving the steady-state PBHE when a set of values $\boldsymbol{\xi}_a$ (see Section 3.3) is assigned to the selected parameters, the reconstruction method is applied assuming that $\mathcal{F}(\mathbf{r};\boldsymbol{\xi}_a)$ is known only at the spatial points $\mathbf{q}_\ell$, $\ell = 1,\ldots,L$, located along the direction of the catheter and affected by a normally distributed noise $f_\mathcal{N}(\mathbf{q}_\ell;\, \mu, \sigma^2)$ [4].

Figure 4.2 shows a typical visualization of the reconstruction error for a randomly selected target map, when the considered catheter case is the second one (Section 4.1). Alongside it, a box plot summarizes the variability of thermal parameters set (k and ω): for each relevant tissue identified within the ROI, it reports the minimum, maximum, median, and interquartile range (25th–75th percentiles) of mentioned properties, showing how the parameters of the target set (blue) deviate from the baseline ones (red).
The plot of the normalized goodness function $g(\chi)$ (see Eq. (3.8)) quantifies the fraction of the ROI where the absolute difference between the target and the reconstructed temperature maps is below a specific threshold χ (x-axis). The blue dotted line corresponds to the noiseless reconstruction of the target map; the red dotted line shows the error between the target field and the baseline map, while horizontal black dotted line identifies the 95% of the ROI. The blue shaded region, instead, encloses 1000 Gaussian perturbations ($\mu = \pm 0.1\,^\circ\mathrm{C}$, $\sigma = 0.2\,^\circ\mathrm{C}$) applied to the target map to introduce measurement noise, with the blue dashed line denoting its average [4].

In this study, the reconstruction of three target maps $\mathcal{F}(\mathbf{r};\boldsymbol{\xi}_a)$, $a = 1, 2, 3$ has been performed. In Figure 4.3 temperature maps obtained by solving the steady-state PBHE using parameters from target sets $\boldsymbol{\xi}_1$, $\boldsymbol{\xi}_2$ and $\boldsymbol{\xi}_3$ are reported, alongside with boxplots showing distributions of their thermal parameters.

Figure 4.4 - and continuation of it (Figure 4.5) - reports the results obtained by applying the reconstruction method to the three target maps $\mathcal{F}_1(\mathbf{r};\, \xi_1)$, $\mathcal{F}_2(\mathbf{r};\, \xi_2)$ and $\mathcal{F}_3(\mathbf{r};\, \xi_3)$ for the seven catheter configurations introduced in Section 4.1, with 1000 realizations of Gaussian noise.

Regarding goodness functions $g(\chi)$ for target map $\mathcal{F}_1(\mathbf{r};\, \xi_1)$ (Figure 4.4 and Figure 4.5, left column), in all cases the reconstruction curves (blue) lie well above the reference curve (red) over the whole range of thresholds χ. Since this curve is the one obtained with the SoA approach, its different behavior with respect to the blue curve shows a clear improvement in the reconstructed temperature distribution.
Curves displayed show that in 95% - or even more - of the ROI, the resulting error by reconstructing this target map is on average lower than 0.4 °C for all the invasive catheter cases (2-7), whereas the reference solution reaches significantly higher values (1°C). Moreover, a particularly encouraging outcome is achieved with

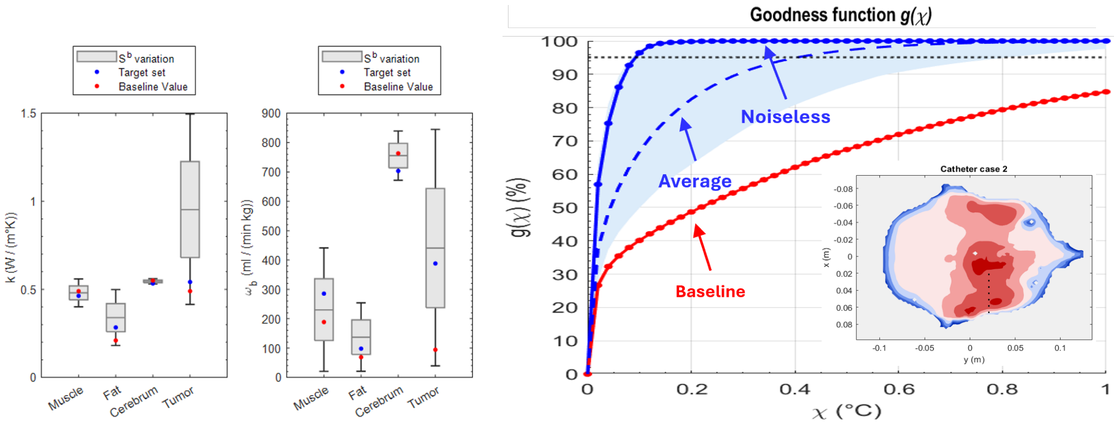

(a) **(b)**

Figure 4.2: Example of parameters boxplots and reconstruction error for a random target map, tested on catheter case 2. a Boxplots show the distribution of the considered sets of thermal parameters (k and ω) corresponding to key tissues in the ROI (muscle, fat, cerebrum and tumor); superimposed blue dots represent the combinations of parameters $\boldsymbol{\xi}_a$ of the target maps, while red dots denote baseline values. **b** Normalized goodness function $g(\chi)$ (see Equation (3.8)): the blue-dot line corresponds to the reconstruction of the target map without noise; blue-shadow area represents the reconstruction of the target map with 1000 realizations of Gaussian noise (with $\mu = \pm 0.1\,°\mathrm{C}$, $\sigma = 0.2\,°\mathrm{C}$), whose mean is indicated by the blue dashed line; red-dot line denotes discrepancy between target map and baseline map.

the least invasive catheter case (case 1, passing through the nose), for which the error obtained with this reconstructing approach is, on average, equal to 0.4 °C over 95% of the ROI. This indicates that, independently of the specific catheter path, the method is able to recover an accurate temperature field for this target map.

Results concerning the goodness function $g(\chi)$ for target map 2 (Figure 4.4 and Figure 4.5, central column) are even more encouraging. Compared with target map 1, all curves are steeper: only catheter cases 1, 5 and 7 show an average error slightly higher than $\chi = 0.2\,°\mathrm{C}$ for 95% of the ROI, whereas all the other configurations achieve $g(\chi) \geq 95\%$ for even $\chi \leq 0.2°\mathrm{C}$. This clearly indicates an overall very high reconstruction accuracy.

For the third and last target map $\mathcal{F}_3(\mathbf{r};\, \xi_3)$, the behavior of the goodness function is again favorable across all catheter configurations. For each case, the reconstruction curve remains above the baseline curve over the whole range of thresholds χ. Analyzing the reconstruction curves, results are similar to those obtained for the

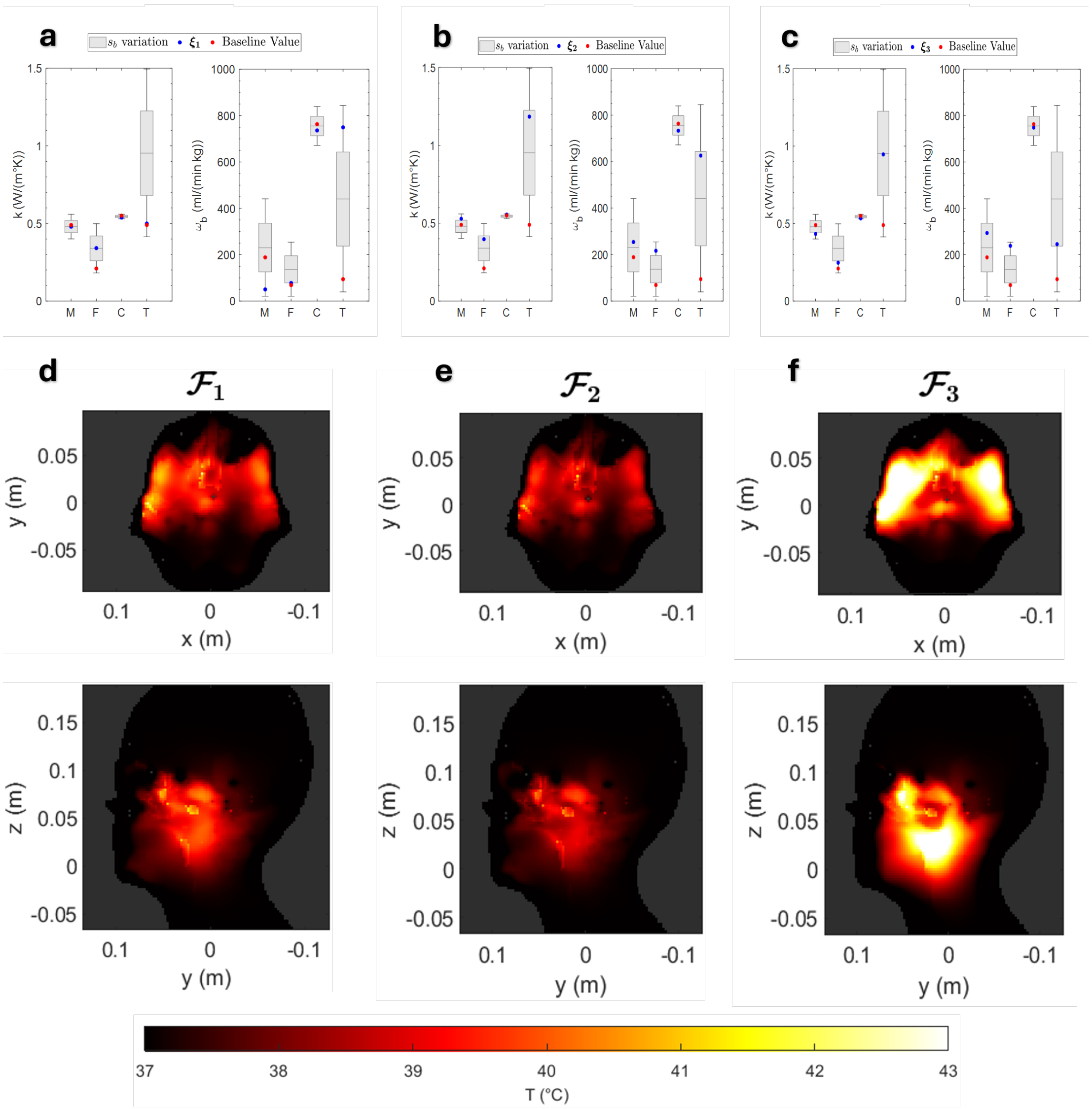

Figure 4.3: Target set temperature maps. a-c Boxplots displaying the range of thermal parameters of each considered target set $\boldsymbol{\xi}_a$, as in the example Figure 4.2a (M = muscle, F = fat, C = cerebrum, T = tumor). **d-f** Temperature field maps corresponding to: (**d**) the target set $\boldsymbol{\xi}_1$; (**e**) the target set $\boldsymbol{\xi}_2$ and (**f**) the target set $\boldsymbol{\xi}_3$. Maps are displayed on the xy plane (central row) and yz plane (lower row), each passing through the centroid of the tumor.

first target map: 95% of the ROI exhibits a mean error bounded by $\chi = 0.4\,°\mathrm{C}$ for almost all configurations, with the only exceptions being catheter cases 1 and 7, for which the reconstruction average error nevertheless remains below 0.6°C. This is a remarkable result, especially considering that $\mathcal{F}_3(\mathbf{r};\, \xi_3)$ exhibits a more heterogeneous temperature pattern with pronounced hot spots compared with the other target maps (Figure 4.3).

Moreover, the shaded blue area, representing the variability over different noise realizations on the catheter temperatures, remains quite narrow for the different

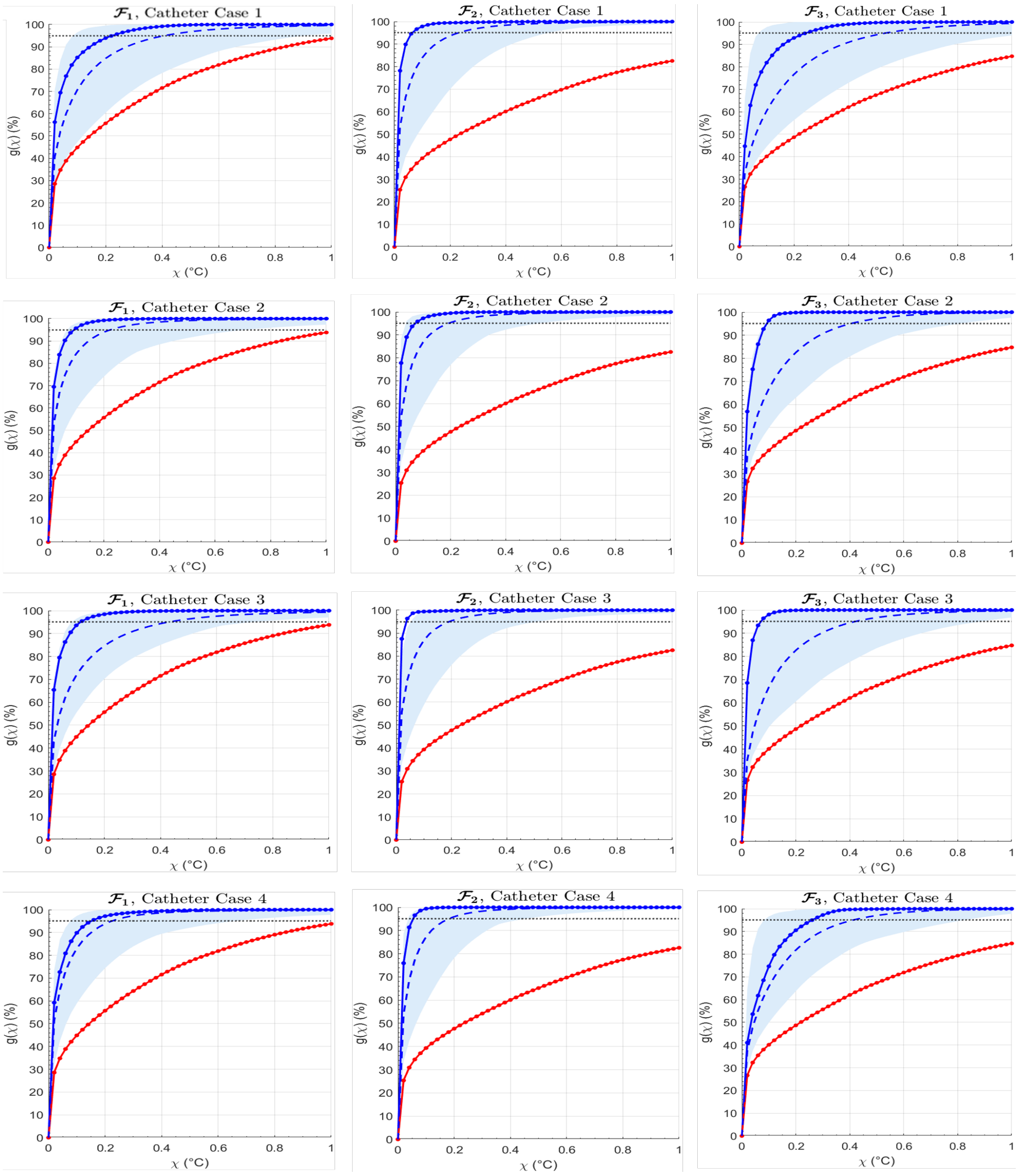

Figure 4.4: Normalized goodness function $g(\chi)$ - as in Figure 4.2b - for the respective target map, each row refer to the different considered catheter cases.

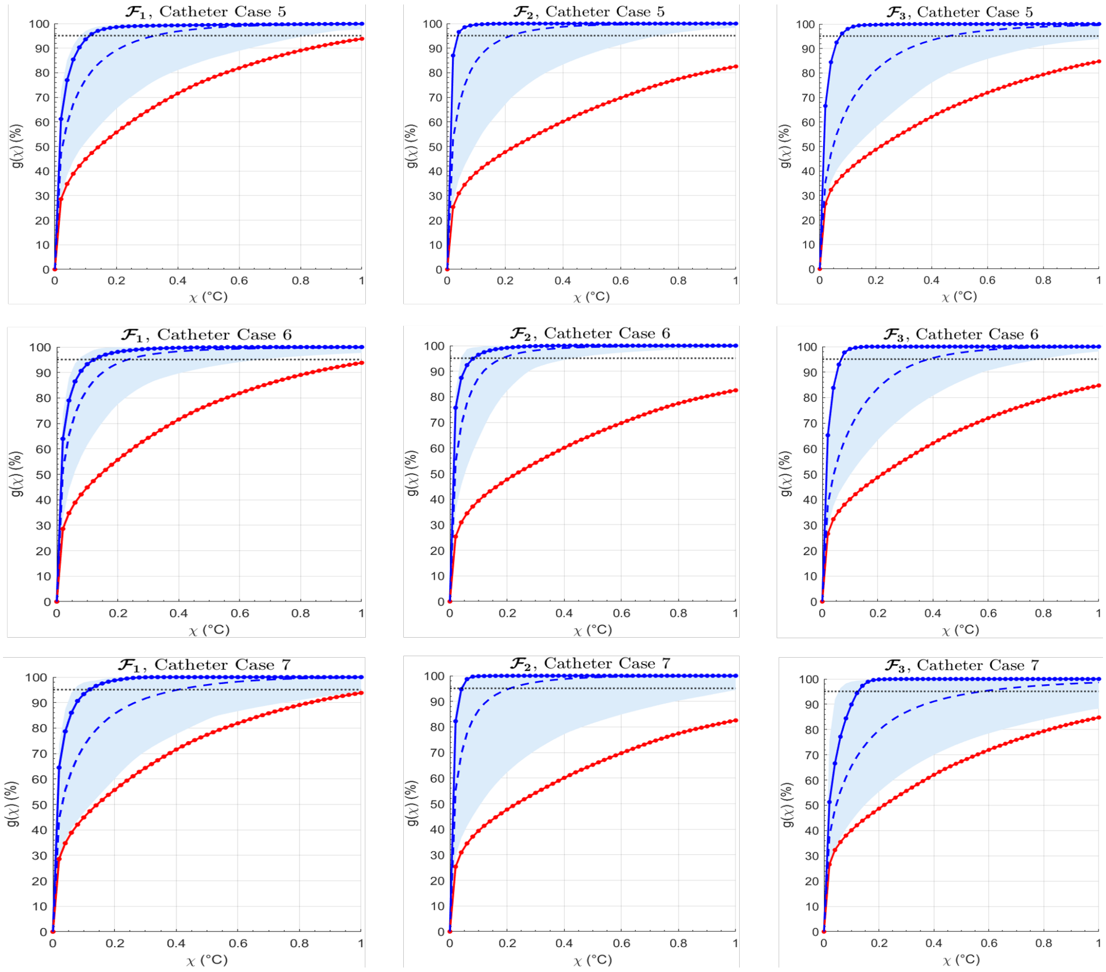

Figure 4.5: Continuation of Figure 4.4.

target maps in each catheter case, which confirms that the reconstruction shows itself to be extremely robust with respect to measurement noise, almost independently of the specific configuration tested.

Finally, an important aspect to underline is that the achieved error is consistently and significantly lower, for every configuration, than the error that would be obtained by simply using the baseline values (red-dotted line).

Discussion

This thesis has addressed one of the main drawbacks to the widespread application of microwave hyperthermia: the lack of reliable real-time temperature monitoring during treatment, especially for deep tumors such as in the H&N case. Working with the standardized ESHO benchmark framework [1] and using the Alex H&N model [21], a complete numerical pipeline was developed from patient-specific EM–thermal modeling and SAR optimization to the implementation of the library-based temperature reconstruction method, driven by sparse and noisy catheter measurements, proposed by Gaffoglio et al. [4].

The initial part of the thesis consisted in reproducing the ESHO Alex benchmark case as faithfully as possible. To this purpose, the realistic anatomical model of Alex was imported into Sim4Life; the benchmark H&N applicator was implemented, and dielectric and thermal tissue properties were assigned, following the ESHO guidelines and adopting thermal stress conditions for malignant tissues. A coupled EM–thermal simulation chain was set up: multiport FDTD simulations were employed to compute stand-alone fields and SAR patterns that were then combined and used as input sources for steady-state thermal simulations based on Pennes' bioheat equation. Using antenna feeding coefficients derived from the temperature-based optimization and provided within the ESHO benchmark dataset, SAR and temperature distributions were first reproduced and compared against the reference maps reported in the ESHO database.
This analysis revealed that, with a normalized input power of 300 W, the benchmark configuration achieved poor SAR focusing with suboptimal temperatures in the target region, requiring higher power levels - of the order of 500 W - to reach the ESHO thermal targets for the given model. This observation led to the adoption of a SAR-based optimization methodology aimed at emphasizing the focusing efficiency and reducing the deposition of power in undesired areas.

The second part of the work entailed using a PSO algorithm, implemented in Matlab, in order to determine optimal amplitude and phase excitations for the twelve antennas. Resulting feeding coefficients were used to set up a new baseline configuration for which SAR and temperature maps were evaluated. SAR maps demonstrated stronger and more localized power deposition in the tumor, while previously observed hot spots in nose, mouth and chin were reduced or eliminated. The corresponding temperature distributions showed higher intratumoral peaks and better confinement of the heated region. Lowering the input power to 290 W, both safety and efficacy conditions recommended by ESHO were fulfilled: T50 exceeded 40 °C in the HTV, and maximum temperatures remained below 44 °C in both tumor and healthy tissues. This configuration was therefore adopted as the baseline map used throughout the reconstruction study.

Building on this baseline, the core of the thesis was the application of the temperature reconstruction method that included several steps. First, the identification of relevant tissues within the H&N volume of interest has been performed: muscle, fat, cerebrum, and tumor were chosen according to spatial prevalence and thermosensitivity. Then, spanning thermal conductivity k and blood perfusion ω for these tissues, parameters' space was defined, with Sobol sequence used to generate a multigrid of 256 parameters' different combinations. By mutating the chosen parameters when all the other properties maintain their baseline value, the patient-specific library of temperature maps is thus generated; this required running a large set of steady-state thermal simulations in Sim4Life. On this basis, a constrained least-squares inversion scheme has been implemented: it reconstructed the temperature field in the ROI as a convex combination of B = 70 basis maps - taken as reconstruction functions - fitting a limited set of noisy measurements sampled along catheter trajectories. In particular, for this thesis we decided to apply this method to three target maps, testing seven different catheter configurations and introducing 1000 realizations of Gaussian noise, with mean systematic noise $\mu = \pm 0.1$°C and standard deviation $\sigma = 0.2$°C.

These reconstruction results indicate that the library-based method can reconstruct accurate 3D temperature distributions in the ROI from very limited, noisy data. For the three target maps and all seven catheter configurations considered, 95% of the ROI shows an average reconstruction error between 0.2 °C and 0.4 °C, consistently outperforming the SoA simulation-based approach.
Importantly, even the least-invasive configuration—a purely nasal catheter that does not cross the tumor volume—provides average errors below 0.6 °C over 95% of the ROI for all target maps, indicating that the method can provide clinically meaningful volumetric information with very limited invasiveness.

Conclusions

The reconstruction method implemented constitutes an effective solution to the problem of temperature monitoring, since various aspects of its workflow and results achieved contribute to its reliability and robustness. First, it overcomes some of the most important limitations of MR thermometry, such as high operating costs and sensitivity to motion. It is not heavily influenced by typical catheter measurement uncertainties, having demonstrated robustness against multiple realizations of Gaussian noise; it also reaches accuracy comparable to the optimization-based methods so far proposed in literature, while operating in real time [4].
Besides, by changing k and ω for the most relevant tissues over wide ranges, the library spans the plausible variability in tissue thermal response, probably the dominant source of uncertainty in hyperthermia treatments. In the specific benchmark considered in this thesis, the proposed approach outperforms SoA methods that rely on fixed literature parameter values and performs well for both invasive and minimally invasive trajectories, with different orientations and sampling densities. Within the constraints of the benchmark setting, these results indicate that the reconstruction method is a reliable candidate for real-time 3D temperature monitoring in microwave hyperthermia.

Despite these promising results, a few important limitations of the followed approach have to be emphasized. First, the study in this thesis was limited to only one virtual patient (Alex) and only for a specific anatomical site - a H&N nasopharyngeal tumor - so the performance of the method can be different for various anatomies, locations of the tumor and applicator designs.
In addition, the bioheat equation was solved under steady-state conditions, neglecting dynamics in heating/cooling and time-dependent perfusion changes. In clinical treatments the transient effects - possibly due to changes in the direction and velocity of blood flow - and thermal dose accumulation are two key factors that may significantly impact the clinical outcome. Furthermore, only thermal parameters were varied in this work, while dielectric properties can also be an important source of uncertainty.

The results of this thesis open several perspectives for further research and development. A natural first step, as already performed in [4], is to shift from steady-state to time-dependent simulations for the current ESHO benchmark models, including temperature-dependent perfusion and material properties. This extension would allow reconstruction of the dynamic evolution of temperature and a more direct integration with thermal dose metrics.
In this work we focused on the H&N region, a challenging site due to tissue heterogeneity and the presence of thermosensitive regions; however, the same workflow could be extended to a broader set of patients, other tumor sites, and alternative applicator designs. Gaffoglio et al. [4] already implemented the reconstruction method on two different phantoms of the Sim4Life virtual population [39], so a particularly interesting future perspective would be to apply and validate the proposed approach on as many virtual models already available in the literature as possible, thereby helping to identify anatomical configurations or treatment scenarios in which reconstruction becomes more challenging.

In conclusion, this thesis demonstrated that patient-specific, library-based temperature reconstruction can provide accurate volumetric thermometry in microwave hyperthermia using only sparse, noisy catheter measurements within a rigorously standardized benchmark framework. The proposed methodology will open up ways toward less invasive, more reliable, and more efficient temperature monitoring in hyperthermia treatments by combining SAR-based optimization with a robust reconstruction algorithm which explicitly takes tissue-property uncertainty into account, representing a promising step toward safer and more effective clinical implementation.

Bibliography

[1] Margarethus M. Paulides, Dario B. Rodrigues, Gennaro G. Bellizzi, Kemal Sumser, Sergio Curto, Esra Neufeld, Hazael Montanaro, H. Petra Kok, and Hana Dobsicek Trefna. «ESHO benchmarks for computational modeling and optimization in hyperthermia therapy». In: *International Journal of Hyperthermia* 38.1 (Jan. 1, 2021), pp. 1425–1442. ISSN: 0265-6736, 1464-5157.

[2] H. Petra Kok and Johannes Crezee. «Hyperthermia Treatment Planning: Clinical Application and Ongoing Developments». In: *IEEE Journal of Electromagnetics, RF and Microwaves in Medicine and Biology* 5.3 (Sept. 2021), pp. 214–222. ISSN: 2469-7249, 2469-7257.

[3] Gerard C. Van Rhoon and Peter Wust. «Introduction: Non-invasive thermometry for thermotherapy». In: *International Journal of Hyperthermia* 21.6 (Sept. 1, 2005), pp. 489–495. ISSN: 0265-6736, 1464-5157.

[4] Rossella Gaffoglio et al. «Real-time 3D temperature reconstruction in microwave cancer hyperthermia from scarce temperature measurements». In: *Nature Communications* 16.1 (May 24, 2025), p. 4824. ISSN: 2041-1723.

[5] Maryam Firuzalizadeh et al. «Joint Optimization of Antenna System Matching and Specific Absorption Rate Focusing in Microwave Hyperthermia Cancer Treatment». In: *Cancers* 17.3 (Jan. 24, 2025), p. 386. ISSN: 2072-6694.

[6] N.R. Datta, S. Gómez Ordóñez, U.S. Gaipl, M.M. Paulides, H. Crezee, J. Gellermann, D. Marder, E. Puric, and S. Bodis. «Local hyperthermia combined with radiotherapy and-/or chemotherapy: Recent advances and promises for the future». In: *Cancer Treatment Reviews* 41.9 (Nov. 2015), pp. 742–753. ISSN: 03057372.

[7] Paula Soares, Isabel Ferreira, Rui Igreja, Carlos Novo, and J.P. Borges. «Application of Hyperthermia for Cancer Treatment: Recent Patents Review». In: *Recent Patents on CNS Drug Discovery* 7 (Aug. 2011), pp. 64–73.

[8] Piotr Gas. «Essential Facts on the History of Hyperthermia and their Connections with Electromedicine». In: *Przeglad Elektrotechniczny* (2017). Publisher: arXiv Version Number: 1.

[9] M.M. Paulides, H. Dobsicek Trefna, S. Curto, and D.B. Rodrigues. «Recent technological advancements in radiofrequency- andmicrowave-mediated hyperthermia for enhancing drug delivery». en. In: *Adv. Drug Deliv. Rev.* 163-164 (2020), pp. 3–18. ISSN: 0169409X.

[10] Akke Bakker, Jacoba Van Der Zee, Geertjan Van Tienhoven, H. Petra Kok, Coen R. N. Rasch, and Hans Crezee. «Temperature and thermal dose during radiotherapy and hyperthermia for recurrent breast cancer are related to clinical outcome and thermal toxicity: a systematic review». In: *International Journal of Hyperthermia* 36.1 (Jan. 1, 2019), pp. 1023–1038. ISSN: 0265-6736, 1464-5157.

[11] G. Lassche, J. Crezee, and C.M.L. Van Herpen. «Whole-body hyperthermia in combination with systemic therapy in advanced solid malignancies». In: *Critical Reviews in Oncology/Hematology* 139 (July 2019), pp. 67–74. ISSN: 10408428.

[12] Margarethus M. Paulides, Gerda M. Verduijn, and Netteke Van Holthe. «Status quo and directions in deep head and neck hyperthermia». In: *Radiation Oncology* 11.1 (Dec. 2016), p. 21. ISSN: 1748-717X.

[13] M. M. Paulides, J. F. Bakker, E. Neufeld, J. Van Der Zee, P. P. Jansen, P. C. Levendag, and G. C. Van Rhoon. «The HYPERcollar: A novel applicator for hyperthermia in the head and neck». In: *International Journal of Hyperthermia* 23.7 (Jan. 2007), pp. 567–576. ISSN: 0265-6736, 1464-5157.

[14] A.L. Oei, H.P. Kok, S.B. Oei, M.R. Horsman, L.J.A. Stalpers, N.A.P. Franken, and J. Crezee. «Molecular and biological rationale of hyperthermia as radio- and chemosensitizer». In: *Advanced Drug Delivery Reviews* 163-164 (2020), pp. 84–97. ISSN: 0169409X.

[15] Maryam Firuzalizadeh, Rossella Gaffoglio, Giorgio Giordanengo, Marco Righero, and Giuseppe Vecchi. «Specific Absorption Rate Optimization in Microwave Cancer Hyperthermia via Local Power Synthesis Algorithm». In: *Cancers* 17.17 (Aug. 28, 2025), p. 2813. ISSN: 2072-6694.

[16] John David Jackson. *Classical electrodynamics*. 3rd. New York, NY: John Wiley & Sons, Ltd, 1999. ISBN: 9780471309321.

[17] Fatemeh Adibzadeh, Margarethus M. Paulides, and Gerard C. Van Rhoon. «SAR thresholds for electromagnetic exposure using functional thermal dose limits». In: *International Journal of Hyperthermia* 34.8 (Nov. 17, 2018), pp. 1248–1254. ISSN: 0265-6736, 1464-5157.

[18] Margarethus M. Paulides, Paul R. Stauffer, Esra Neufeld, Paolo F. Maccarini, Adamos Kyriakou, Richard A.M. Canters, Chris J. Diederich, Jurriaan F. Bakker, and Gerard C. Van Rhoon. «Simulation techniques in hyperthermia treatment planning». In: *International Journal of Hyperthermia* 29.4 (June 1, 2013), pp. 346–357. ISSN: 0265-6736, 1464-5157.

[19] J J W Lagendijk. «Hyperthermia treatment planning». In: *Physics in Medicine & Biology* (2000).

[20] Harry H Pennes. «Analysis of Tissue and Arterid Blood Temperatwes». In: *J. Appl. Physiol.* (1948).

[21] Gennaro G. Bellizzi, Kemal Sumser, Iva VilasBoas-Ribeiro, Sergio Curto, Tomas Drizdal, Gerard C. Van Rhoon, Martine Franckena, and Margarethus M. Paulides. «Standardization of patient modeling in hyperthermia simulation studies: introducing the *Erasmus Virtual Patient Repository*». In: *International Journal of Hyperthermia* 37.1 (Jan. 1, 2020), pp. 608–616. ISSN: 0265-6736, 1464-5157.

[22] Jort A. Groen, Johannes Crezee, Hanneke W.M. Van Laarhoven, Maarten F. Bijlsma, and H. Petra Kok. «Quantification of tissue property and perfusion uncertainties in hyperthermia treatment planning: Multianalysis using polynomial chaos expansion». In: *Computer Methods and Programs in Biomedicine* 240 (Oct. 2023), p. 107675. ISSN: 01692607.

[23] J. B. Van De Kamer, N. Van Wieringe. «The significance of accurate dielectric tissue data for hyperthermia treatment planning». In: *International Journal of Hyperthermia* 17.2 (Jan. 2001), pp. 123–142. ISSN: 0265-6736, 1464-5157.

[24] Peter Wust, Johanna Gellermann, Christian Harder, Wolfgang Tilly, Beate Rau, Stefan Dinges, Peter Schlag, Volker Budach, and Roland Felix. «Rationale for using invasive thermometry for regional hyperthermia of pelvic tumors». In: *International Journal of Radiation Oncology*Biology*Physics* 41.5 (July 1998), pp. 1129–1137. ISSN: 03603016.

[25] Peter Wust, Chie Hee Cho, Bert Hildebrandt, and Johanna Gellermann. «Thermal monitoring: Invasive, minimal-invasive and non-invasive approaches». In: *International Journal of Hyperthermia* 22.3 (Jan. 1, 2006), pp. 255–262. ISSN: 0265-6736, 1464-5157.

[26] Fatemeh Adibzadeh, Kemal Sumser, Sergio Curto, Desmond T. B. Yeo, Amir A. Shishegar, and Margarethus M. Paulides. «Systematic review of pre-clinical and clinical devices for magnetic resonance-guided radiofrequency hyperthermia». In: *International Journal of Hyperthermia* 37.1 (Jan. 1, 2020), pp. 15–27. ISSN: 0265-6736, 1464-5157.

[27] René F. Verhaart, Valerio Fortunati, Gerda M. Verduijn, Aad Van Der Lugt, Theo Van Walsum, Jifke F. Veenland, and Margarethus M. Paulides. «The relevance of MRI for patient modeling in head and neck hyperthermia treatment planning: A comparison of CT and CT-MRI based tissue segmentation on simulated temperature». In: *Medical Physics* 41.12 (Dec. 2014), p. 123302. ISSN: 0094-2405, 2473-4209.

[28] ZMT Zurich MedTech AG. *Sim4Life*. Version v7.0. Electromagnetic and thermal simulation platform. 2024.

[29] The MathWorks Inc. *MATLAB*. Version R2023a. 2023.

[30] Christian Rossmanna and Dieter Haemmerich. «Review of Temperature Dependence of Thermal Properties, Dielectric Properties, and Perfusion of Biological Tissues at Hyperthermic and Ablation Temperatures». In: *Critical Reviews in Biomedical Engineering* 42.6 (2014), pp. 467–492. ISSN: 0278-940X.

[31] IT'IS Foundation. *Tissue Properties Database*. 2025. URL: `https://itis.swiss/virtual-population/tissue-properties/database/`.

[32] William T. Joines, Yang Zhang, Chenxing Li, and Randy L. Jirtle. «The measured electrical properties of normal and malignant human tissues from 50 to 900 MHz.» In: *Medical physics* 21 4 (1994), pp. 547–50.

[33] Tomás Drízdal, Paolo Togni, L Visek, and J Vrba. «Comparison of Constant and Temperature Dependent Blood Perfusion in Temperature Prediction for Superficial Hyperthermia». In: *Radioengineering* (2010).

[34] C Guiot, E Madon, D Allegro, P G Piantà, B Baiotto, and P Gabriele. «Perfusion and thermal field during hyperthermia. Experimental measurements and modelling in recurrent breast cancer». In: *Physics in Medicine and Biology* 43.10 (Oct. 1, 1998), pp. 2831–2843. ISSN: 0031-9155, 1361-6560.

[35] Zef Rijnen, Jurriaan F. Bakker, Richard A.M. Canters, Paolo Togni, Gerda M. Verduijn, Peter C. Levendag, Gerard C. Van Rhoon, and Margarethus M. Paulides. «Clinical integration of software tool VEDO for adaptive and quantitative application of phased array hyperthermia in the head and neck». In: *International Journal of Hyperthermia* 29.3 (May 2013), pp. 181–193. ISSN: 0265-6736, 1464-5157.

[36] H. P. Kok, A. N. T. J. Kotte, and J. Crezee. «Planning, optimisation and evaluation of hyperthermia treatments». In: *International Journal of Hyperthermia* 33 (Aug. 18, 2017). ISSN: 0265-6736, 1464-5157.

[37] J. Kennedy and R. C. Eberhart. «Particle swarm optimization». In: *IEEE International Conference on Neural Networks*. Vol. 4. 1995.

[38] René F. Verhaart, Gerda M. Verduijn, Valerio Fortunati, Zef Rijnen, Theo Van Walsum, Jifke F. Veenland, and Margarethus M. Paulides. «Accurate 3D temperature dosimetry during hyperthermia therapy by combining invasive measurements and patient-specific simulations». In: *International Journal of Hyperthermia* 31.6 (2015), pp. 686–692. ISSN: 0265-6736, 1464-5157.

[39] Marie-Christine Gosselin et al. «Development of a new generation of high-resolution anatomical models for medical device evaluation: the Virtual Population 3.0». In: *Physics in Medicine & Biology* 59.18 (Aug. 2014). Publisher: IOP Publishing, p. 5287.